Journal of Hydrology 590 (2020) 125140

Contents lists available at ScienceDirect

Journal of Hydrology

journal homepage: www.elsevier.com/locate/jhydrol

Research papers

Potential evaporation dynamics over saturated bare soil and an open water surface

Wanxin Li[a,b], Philip Brunner[c], Harrie-Jan Hendricks Franssen[d], Zhi Li[e], Zhoufeng Wang[a,b], Zhengyu Zhang[a,b], Wenke Wang[a,b,*]

[a] Key Laboratory of Subsurface Hydrology and Ecological Effects in Arid Region, Chang'an University, Ministry of Education, PR China
[b] School of Water and Environment, Chang'an University, PR China
[c] Center for Hydrogeology and Geothermics, (CHYN), Université de Neuchâtel, Switzerland
[d] Agrosphere (IBG-3), Forschungszentrum Jülich GmbH, Jülich, Germany
[e] Xi'an Research Institute of China Coal Technology & Engineering Group Corp, PR China

ARTICLE INFO

This manuscript was handled by Huaming Guo, Editor-in-Chief

Keywords:
Potential evaporation
Saturated bare soil evaporation
Open water evaporation
Energy balance equation
Lysimeter

ABSTRACT

Actual evaporation (E_a) can be calculated as a fraction of potential evaporation (PE), which refers to the evaporation rate if supply water is unlimited. Potential evaporation depends on the available energy and the underlying material, and different approaches to estimate potential evaporation exist nowadays. This study provides a detailed analysis of the evaporation dynamics over fully saturated, sandy soil (PE_s) and an open water surface (PE_w). Moreover, the performance of commonly used methods to estimate PE is assessed. At the basis of these analyses is a lysimeter experiment in the Guanzhong Basin, China, which allowed a precise measurement of PE with a very high temporal resolution. Temperature profiles in lysimeters and meteorological data were also measured during the experiment. A comparison of PE_s and PE_w was carried out for seven consecutive days (August 11th to 17th, 2016). Results show that PE_w is smaller than PE_s on a daily scale, with PE_w rates being bigger than PE_s at night but smaller during daytime. Furthermore, the temporal dynamics of PE_w lags 4–5 h behind PE_s. In accordance with the energy balance equation, PE dynamics are mainly governed by "available energy". The PE rates calculated by Penman-Monteith (PM) and Priestly-Taylor (PT) based on these measurements were also evaluated. The measured PE is relatively well reproduced by PM and PT equations. Finally, the effect of using different approaches to estimate PE on calculating E_a was tested by an integrated hydrological model that calculates water flow in the unsaturated zone by solving the Richards equation. The relative differences were up to 17.5%.

1. Introduction

Evaporation is the physical process by which liquid water is transferred to the gaseous state of water vapor (Jensen and Allen, 2016). Evaporation has been extensively studied in hydrology, agricultural sciences, and meteorology, and is of critical importance to the hydrological cycle (Morton, 1994; Burt et al., 2005; Trenberth et al., 2009; Or et al., 2013). Directly measuring actual evaporation rates (E_a) is challenging (Bavel, 1966; Zhidong et al., 1988; Verhoef and Campbell, 2005; Wang and Dickinson, 2012; Lensky et al., 2018). Various methods are available to measure evaporation rates (Table a, Appendix). A widely used approach in agricultural sciences is the Bowen ratio energy balance method. It requires accurate measurements of vertical gradients of air temperature, humidity and net radiation to obtain the latent heat flux for evaporation (LE) and sensible heat flux (H) (Tanner, 1988; Devitt et al., 1998; Kahler and Brutsaert, 2006). However, the Bowen ratio approach is associated with several uncertainties. In addition to random and instrumental errors, errors related to simplifying assumptions in the underlying theory cause biases. For example, the diffusivities of heat and moisture are assumed to be

Abbreviations: PE_s, PE_w, potential evaporation from fully saturated soil and from water; ET_0, reference evapo(transpi)ration; $E_{a,s}$, $E_{a,w}$, actual evaporation rate calculated from PE_s and PE_w (mm/day); LE_s, LE_w, latent heat for saturated soil evaporation and water evaporation (W/m^2); $LE_{measured}$, $LE_{calculated}$, measured and calculated latent heat flux (W/m^2); PM, The Penman-Monteith equation; PT, The Priestly-Taylor equation; LE_{energy}, LE_{aero}, energy and aerodynamic term for evaporation in PM model (W/m^2); G_s, soil heat flux (W/m^2); N_w, the change of heat storage in the water (W/m^2); H_s, H_w, sensible heat flux for saturated soil and for water (W/m^2); $R_{n,s}$, $R_{n,w}$, net radiation for saturated soil and for water (W/m^2); G_h, horizontal heat flux (W/m^2)

* Corresponding author at: School of Water and Environment, Chang'an University, Yanta Road 126, 710054, Xi'an, Shaanxi, PR China.
E-mail address: wenkew@chd.edu.cn (W. Wang).

https://doi.org/10.1016/j.jhydrol.2020.125140
Received 7 September 2019; Received in revised form 3 April 2020; Accepted 1 June 2020
Available online 10 July 2020
0022-1694/

equal and the energy storage is neglected (Blad and Rosenberg, 1974; Angus and Watts, 1984; Gavilán and Berengena, 2007).

Another method is the Eddy Covariance (EC) method which measures LE and H using high-frequency sensors (Tanner, 1988; Verhoef and Campbell, 2005; Wang and Dickinson, 2012). It is one of the main methods to measure evaporation rates, despite the high installation and maintenance cost and problems related to closing the energy balance (e.g., Wilson et al., 2002; Franssen et al., 2010). Besides, EC-measurements are affected by large random errors (e.g., Hollinger and Richardson, 2005; Richardson et al., 2006; Kessomkiat et al., 2013) thus resulting in large uncertainties for hourly estimates of E_a. Stable estimates of evaporation rates by EC can only be calculated over three hours of measurement, depending on the site-specific conditions (Culf et al., 2004; Mahrt, 2010; Huntington et al., 2011; Kessomkiat et al., 2013).

An alternative for estimating evaporation is using lysimeters. Lysimeters allow to directly measure evaporation rates even over short time periods (Hellwig, 1973; Holmes, 1984; Scanlon et al., 1997; Goss and Ehlers, 2010; Jensen and Allen, 2016; Pütz et al., 2018). Despite their high accuracy, lysimeters are not routinely used because of the high installation cost, random errors related for example to measurement uncertainty. Especially in arid regions, they are rarely used. Also, lysimeter data are not necessarily representive for larger regions.

As an alternative approach to directly estimating E_a, a commonly used strategy is to estimate potential evaporation rate (PE) first, and on this basis calculate E_a. This approach is more extensively used compared to the above-mentioned methods because it is based on meteorological data which are widely and readily available. The ratio between E_a and PE depends on factors such as soil type, soil water availability (Federer et al., 1996; Kirono et al., 2010), atmospheric resistance, heat conductance (Mcilroy, 1984) and radiative properties (Mahrt and Ek, 1984) of the surface. Numerous methods to estimate PE have been suggested. We loosely assign these methods to the following three categories according to the surface-type:

A. Evaporation from an open water surface (PE_w):

Shuttleworth, for example, defined PE as "*evaporation from an idealized, extensive free water surface*" (Shuttleworth, 1983). Mahrt also defined PE as "*evaporation occurring over a free water surface*", which implies that PE rates are only controlled by the atmospheric conditions (Mahrt and Ek, 1984; Mahrt, 2010). Different approaches to determine PE_w have been developed, for example, Dalton-type equations (consisting of wind speed function and vapor pressure deficit) and so-called combination models such as de Bruin-Keijman equations (Bruin, 1982).

B. Evaporation from a saturated soil surface (PE_s):

The formulation to calculate evaporation from a saturated soil surface was originally proposed by Penman (Penman, 1948). The Penman equation combines meteorological measurements with a surface energy balance. It is one of the most important approaches to estimate PE (McJannet et al., 2013). Based on Penman, van Bavel extended the definition of PE rate as—"*when surface is wet and imposes no restriction upon the flow of water vapor*" (Bavel, 1966). Priestley and Taylor developed a simpler model to estimate PE_s. As opposed to the Penman equation, the aerodynamic term is not considered. Instead, a correction factor to the energy balance is added (Priestley and Taylor, 1972). Menenti and Choudhury also defined PE in relation to the saturated soil surface as "*the rate of liquid to vapour transition which is not affected by the liquid water flow beneath the physical boundary of the evaporating body*" (Menenti and Choudhury, 1993). Milly proposed that E_a is equal to the potential value when the soil has a sufficiently high soil moisture content (Milly, 1992). Brutsaert introduced the apparent potential evaporation rate, and defined it as "*the evaporation rate that would occur if the surface would be well supplied with water*" (Brutsaert, 2013). A completely saturated soil surface is common in wetlands and areas where the depth to groundwater is smaller than the capillary rise height.

C. Potential evaporation for vegetation with fixed geometric and aerodynamic features—Reference Evapo(transpi)ration (ET_0):

This concept also originated from Penman. He combined energy and aerodynamic terms and defined the ET_0 as "*the evaporation rate by a short green crop, which completely shades the ground and is of uniform height, with plenty of water*" (Penman, 1948; Federer et al., 1996). The developed Penman equation is widely used in agricultural and hydrological research, providing a quantitative basis to estimate the crop water requirements such as proposed for example in the FAO58 method (Monteith and Unsworth, 2008).

Calculating E_a on the basis of PE is the most widely implemented approach in many disciplines including hydrogeology (e.g. groundwater modelling), hydrology (watershed modelling) and agricultural applications (estimation of irrigation demand). Different approaches to calculate PE exist, but it is unclear which approach should be used and how large the biases induced in estimating E_a are. In fact, PE_s, PE_w and ET_0 have all been used as a starting point to estimate actual E_a (Granger,1989; Allen et al., 1989; Westra, 2009; Kirono et al., 2010). In addition, E_a can also be calculated based on energy balance considerations and coupling of the water and energy cycles, as is usually done in land surface models and micrometeorological applications. It is assumed that this approach can yield more precise E_a estimates, but it requires more input data than the other PE-based approaches.

The aim of this paper is to provide a quantitative assessment and comparison of approaches to estimate potential evaporation over open water and saturated bare soil, based on the energy balance method and equations to estimate PE (such as the Penman-Monteith and the Priestly-Taylor equations). The basis for this comparison is a unique lysimeter experiment in a warm temperate semi-arid continental monsoon climate near Xi'an (Shaanxi province, Guanzhong Basin, China), in which evaporation rates are measured for a water column and a fully saturated soil column. The lysimeters are operated in a way that allows us to accurately measure evaporation rates with a high temporal discretization: a measurement is taken every half an hour. Given that alternative methods to estimate evaporation rate cannot reach a high temporal resolution, our study is unique. Moreover, to the best of our knowledge, the above-mentioned PE-estimation methods have so far not been compared with precise, hourly measured PE-data. Specifically, the following questions are addressed:

- What are the diurnal dynamics of measured PE for the water column (PE_w) and fully saturated soil column (PE_s)?
- How can the differences be explained from a physical point of view?
- How does the choice of PE-estimation methods (energy balance vs PM and PT methods) compare to measured PE (bare soil vs open water surface)?
- How does the choice of PE affect subsequent estimates of actual evaporation rate E_a in numerical models?

2. Materials and methods

2.1. Study site

The experiment was conducted at the "Semi-arid Groundwater and Environment Experimental Site", located at Chang'an University, Xi'an, China (Latitude: 34°28'N; Longitude: 108°93'E). Lysimeter observation columns (made by fiberglass) are buried and aligned with the ground surface, and all have the same area (1.0 m^2) and height (0.7 m), see Fig. 1. The lysimeters are more than ten meters away from the roadside trees. Note that on the photo in Fig. 1 they appear closer. This is due to the vantage point of the photograph (from the only high-rise building

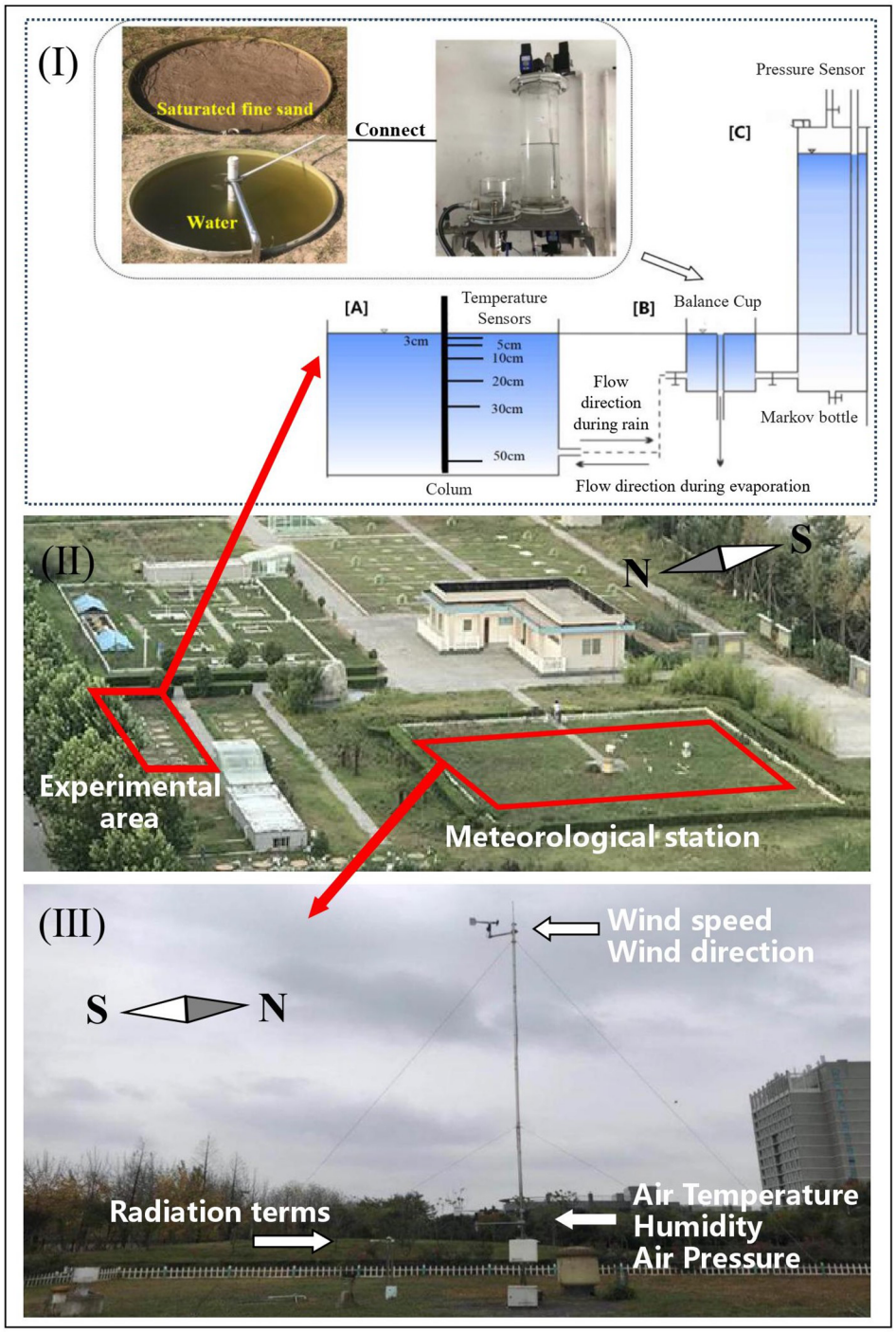

Fig. 1. (I) Setup of the PE measurement device: lysimeter column (A), balance cup (B), the Automatic Water Replenishing Markov Bottle (C); (II) Overview of the experimental site; (III) Measurement setup at the meteorological station. For example, wind speed and wind direction at 10 m, radiation measurement at 1.5 m, air temperature, relative humidity and air pressure measurements at 1.5 m.

Table 1
Particle composition of the fine sand in the lysimeter.

Particle size (mm)	Particle Composition (%)					
	> 2.00	2.00–0.50	0.50–0.125	0.125–0.095	0.0925–0.045	< 0.045
Fine Sand	0	0	93.22	2.87	1.5	2.41

where a panorama photo of the experimental site can be taken).

The observation columns are filled with homogeneous fine sand from the Guanzhong Basin. The particle composition is based on the Standard for Soil Test Method (GB/T50123-1999), shown in Table 1.

2.2. Field measurements

A standard meteorological station is located in the southwestern part of the experimental site, measures air temperature, humidity, net radiation components, wind speed and air pressure. Fig. 1 illustrates the measurement setup including the height of the sensors. All data were logged every 5 min. The commercial names and model of the measurement devices employed are listed in Table b (Appendix).

Temperature sensors (instrument: 5TM and MPS6) are buried at 3, 5, 10, 20, 30 and 50 cm depth in the soil of the lysimeter column (as shown in Fig. 1) and 5, 10, 20, 40, 60 cm depth in the soil out of the lysimeter. Data are automatically recorded by the EM50 data logger every 5 min. Water temperatures are measured at the same depth as in the soil by a resistor temperature sensor (1/3DIN) and also automatically recorded every 5 min.

If a lysimeter has continuous water supply, evaporation is not restricted by water availability, but by the net available energy and environmental conditions (Westra, 2009). We designed our setup in a way that the measured evaporation rate corresponds to the potential evaporation (PE). Direct measurements of potential evaporation for saturated fine sand (PE_s) and water (PE_w) were made by the "Automatic Water Replenishing Markov Bottle". This system was invented by Chang'an University and can provide reliable evaporation data with a high temporal resolution. It got a Utility Model Patent in 2014 (Shen et al., 2014). As shown in Fig. 1, the water table in the columns was maintained at the soil/water surface, which means the water table depth is zero. The Markov Bottle is installed in the basement, connecting the columns with the balance cup. When evaporation takes place, water is rapidly replenished.

The device is based on the principle of connected vessels, and given the principle of mass balance, the water quantity evaporated in the lysimeter column (M_A) equals to the quantity delivered by the Markov bottle (M_C). We can rewrite this as:

$$\pi \cdot r_A^2 \cdot \Delta h_A = \pi \cdot r_C^2 \cdot \Delta h_C \quad (1)$$

where Δh_A is the PE rate of the lysimeter, Δh_C is the water level variation in the Markov Bottle, which can be measured by pressure sensors in the bottle (MPM489, MICROSENSOR, see Fig. 1), r_A (56.5 cm) and r_C (6.0 cm) are the radius of the lysimeter column and the Markov bottle respectively, so that:

$$\Delta h_A = \Delta h_C / 88.7 \quad (2)$$

A drop of the water level in the Markov bottle of 88.7 cm thus coincides with an evaporation rate in the lysimeter column of 1 cm. The set-up allows determining the evaporation with very high accuracy.

A linear statistical analysis was employed to assess the temporal dynamics of PE_s and PE_w in relation to meteorological data.

$$V = \frac{V_i - V_{min}}{V_{max} - V_{min}} \quad (3)$$

where V_i represents a measured PE or a meteorological variable, V_{max} and V_{min} are the maximum and minimum values in the measured time series. The measured data also form the basis for the comparison with the upcoming methods.

2.3. Energy balance

Energy balance approaches are widely used to estimate evaporation rates (Singh and Xu, 2015). The energy balance at the land–atmosphere interface is given by:

$$\begin{aligned} &\text{(a) } R_{n,s} - G_s - H_s = LE_s \quad \text{soil} \\ &\text{(b) } R_{n,w} - G_w - H_w = LE_w \quad \text{water} \end{aligned} \quad (4)$$

where the subscripts s and w refer to fine sand and water respectively. R_n (W/m^2) is the net radiation. N_w (W/m^2) represents the change of heat storage in the water body, and G_s (W/m^2) is soil heat flux. H (W/m^2) is the sensible heat flux and LE (W/m^2) is the latent heat flux for evaporation. R_n, G_s and N_w are positive in the downward direction, while LE and H are positive upwards. The equations for all terms in Eq. (4) are provided in the Appendix (equations 17–31).

Net radiation R_n is different for fine sand and water, owing to their different albedos (equations 17–21 of the Appendix). The sensible heat flux H (calculated through equations 28–31 of the Appendix) is often negative as most of the energy over the lysimeter and water columns is used for evaporation. The Gradient method (Eq. (22)) is considered as a standard method for calculating the soil heat flux G_s (Horton et al., 1983; Evett et al., 2012). Note, however, that it is difficult to measure the temperature at the soil surface. In practice, the gradient method is therefore based on temperature mseasurements in the shallow surface (e.g. between 3 cm and 5 cm below ground in this study). The heat flux within the soil (abbreviated with G_0) is not equivalent to G_s as it neglects heat storage ΔS between the location of the highest sensor and soil surface. This can result in errors up to 10% (Massman, 1993; Heitman et al., 2010). While in practice G_s is often approximated through G_0, we correct this estimate in the following way (An et al., 2017):

$$G_s = G_0 + \Delta S \quad (5)$$

where ΔS is calculated from temporal soil temperature variations (Braud et al., 1993; Roxy et al., 2014). The temperature measured at 3 cm depth is used to estimate ΔS in Eq. (5) (Ochsner et al., 2007), assuming it represents the average temperature in the uppermost surface:

$$\Delta S = \Delta z \cdot c_s \cdot \frac{(T_{i+1} - T_i)}{\Delta t} \quad (6)$$

where the subscript i refers to time, $T_{i+1} - T_i$ (K) is the temporal temperature variation Δz is the layer thickness over which the heat storage is calculated (3 cm in this work), c_s is the soil volumetric heat capacity and equal to 2.19 MJ/m^3K, calculated through Eq. (24), Δt is time step (30 min in this study).

For water, heat storage N_w is a significant component of the energy balance, which can be calculated according to (Gallego-Elvira et al., 2011; McJannet et al., 2013):

$$N_w = \rho_w \cdot c_w \cdot z \cdot (T_{i+1} - T_i)/\Delta t \quad (7)$$

where ρ_w ($1000\ kg \cdot m^{-3}$) is the water density, c_w ($4.2\ kJ \cdot kg^{-1} \cdot K^{-1}$) is the specific heat of water, z (m) is the depth of a water layer (the water column was divided into layers of 10 cm depth to calculate heat storage of water. The temperature used to calculate N_w for each layer is based on linear interpolation), i refers to time, $T_{i+1} - T_i$(K) is the temporal temperature variation, and Δt is the time step (30 min).

One complication of our specific setup is that the net energy balance of the lysimeter is affected by horizontal energy exchange G_h between the lysimeter column and the surroundings. The horizontal heat fluxes for fine sand ($G_{h,s}$) and water ($G_{h,w}$) were estimated based on linear interpolation of measured temperature along vertical profiles inside and outside the lysimeter: ($\bar{T}_{outside} - \bar{T}_{inside,s}$ or $\bar{T}_{outside} - \bar{T}_{inside,w}$). $G_{h,s}$ and $G_{h,w}$ are calculated every 30 min by Eq. (22), with $\lambda_{fiberglass} = 0.4\ W \cdot m^{-1} \cdot K^{-1}$ (Li, 2018), and thickness of the lysimeter wall equivalent to 0.02 m.

For the water column, the horizontal heat flux $G_{h,w}$ is an additional energy term, and we assume that it affects latent heat in the same way as R_n. This is justified given the homogeneous vertical temperature profile for water (see upcoming Fig. 6). For soil, on the other hand, the vertical temperature distribution inside the lysimeter column is not

uniform. The horizontal energy continuing to the soil lysimeter column in the deeper layers will contribute much less to an increase of the latent heat flux than the net radiation available to the upper soil layers. We consider this effect by introducing an exponential-type weighting function as a function of soil depth to estimate the average temperature inside $\bar{T}_{inside,s}$:

$$\bar{T}_{inside,s} = \sum_{j=1}^{50} T_j \cdot y_j \tag{8}$$

where the subscript j refers to depth, T_j corresponds to the soil temperatures at different depths, y_j is calculated in the following way:

$$y_j = e^{-\varphi \cdot j} \tag{9}$$

where y_j represents the weight for the measured soil temperature at a particular depth. φ is the shape parameter which is modified through trial and error to close the energy balance. The value of 0.397 was employed in this study (see Fig. 9). Thus G_h can be calculated as:

$$\begin{aligned} G_{h,s} &= -\lambda_{fiberglass} \cdot \frac{\bar{T}_{outside} - \bar{T}_{inside,s}}{0.02} \\ &= -\lambda_{fiberglass} \cdot \frac{\bar{T}_{outside} - \sum_{j=1}^{50} T_j \cdot e^{-\varphi j}}{0.02} \quad \text{soil} \\ G_{h,w} &= -\lambda_{fiberglass} \cdot \frac{\bar{T}_{outside} - \bar{T}_{inside,w}}{0.02} \quad \text{water} \end{aligned} \tag{10}$$

A further complication of this column experiment is that the water which is replenished to supply evaporation from the Markov bottle (located in the basement of the lysimeter site) has a lower temperature than the soil (water) in the column. The extra energy Q (kJ/d) which is injected in the lysimeter related to this temperature difference ΔT (°C) has to be taken into account, if it is a significant component of the energy balance:

$$Q = c_w \cdot m \cdot \Delta T \tag{11}$$

where $c_w = 4.2$ kJ/(kg·°C) is water heat capacity, m (kg/d) is the water flux which needs to be replenished related to evaporation per day. A detailed assessment of the importance of this component was carried out and showed that the incoming flux only corresponds to about 1–3% of the latent heat. This is related to the fact that the inflowing water flux as well as the temperature difference between the inflowing water and the lysimeter are small. We therefore do not explicitly consider this term in the upcoming analysis.

As shown in Fig. 2, all additional energy terms were added in the energy balance equations for the sand and water lysimeter columns:

$$\begin{aligned} &\text{(a) } G_{h,s} + R_{n,s} - G_s - H_s = LE_s \quad \text{soil} \\ &\text{(b) } G_{h,w} + R_{n,w} - N_w - H_w = LE_w \quad \text{water} \end{aligned} \tag{12}$$

2.4. Penman-Monteith and Priestly-Taylor equations

The performance of widely used methods to estimate potential evaporation was assessed; potential evaporation was calculated according to the Penman-Monteith (PM) and Priestly-Taylor (PT) equations.

The Penman-Monteith model combines both energy (LE_{energy}) and aerodynamic terms (LE_{aero}) for evaporation. It is widely used to estimate both evapotranspiration and evaporation (Mcjannet et al., 2013; Jensen and Allen, 2016). For saturated bare soils or water surfaces r_s (including the canopy resistance r_c) is assumed to be zero as no restriction on evaporation rate occurs (Finch, 2001; Jensen and Allen, 2016. p.625.), the PM equation in this study is:

$$\begin{aligned} LE_s &= \frac{\Delta \cdot (G_{h,s} + R_{n,s} - G_s)}{\Delta + \gamma} + \frac{\rho_a \cdot c_p \cdot (e_s - e_a)/r_{a,s}}{\Delta + \gamma} \quad \text{soil} \\ LE_w &= \frac{\Delta \cdot (G_{h,w} + R_{n,w} - N_w)}{\Delta + \gamma} + \frac{\rho_a \cdot c_p \cdot (e_s - e_a)/r_{a,w}}{\Delta + \gamma} \quad \text{water} \\ LE &= LE_{energy} + LE_{aero} \end{aligned} \tag{13}$$

Δ (kPa/°C) is the gradient of saturation vapor pressure-temperature curve, γ is the psychrometric constant (0.066 kPa/°C), ρ_a is the air density (which is equal to 1.02 kg/m^3), c_p (1010 J·kg^{-1}·K^{-1}) is the specific heat of air, e_s (kPa) is the saturation vapor pressure, e_a (kPa) is the vapor pressure corresponding to air temperature and r_a (s·m^{-1}) is the aerodynamic resistance (see also Appendix, equations 30–31). L the is latent heat for evaporation (2.43 MJ/kg). For water, heat storage N_w instead of G_s is used.

Different from Penman-type equations, the aerodynamic term (LE_{aero}) is simplified by the empirical parameter α_{PT} in the Priestley-Taylor equation (Priestley and Taylor, 1972; Yang and Roderick, 2019):

$$\begin{aligned} \alpha_{PT} &= LE / LE_{energy} \\ LE_s &= \alpha_{PT} \cdot \frac{\Delta \cdot (G_{h,s} + R_{n,s} - G_s)}{\Delta + \gamma} \quad \text{soil} \\ LE_w &= \alpha_{PT} \cdot \frac{\Delta \cdot (G_{h,w} + R_{n,w} - N_w)}{\Delta + \gamma} \quad \text{water} \end{aligned} \tag{14}$$

α_{PT} was empirically determined to be 1.26 for wet surfaces (Stewart and Rouse, 1977; Crago and Brutsaert, 1992; Crago, 1996; Kellner, 2001).

2.5. Hydrological modelling with HydroGeoSphere

Numerical models such as HydroGeoSphere (HGS) are widely applied for applications at the field or catchment scale to simulate surface and subsurface flow processes, including transpiration and evaporation processes, as well as infiltration and capillary rise (Brunner and Simmons, 2012). Potential evaporation is a critical input for these simulations. Here, we explore the influence of potential evaporation on actual evaporation by using PE rates obtained from free water surface and PE obtained in the saturated soil. Actual evaporation dynamics under these different boundary conditions are tested for two soil types (sand and silty clay) for different depths of the water table. We carry out the simulations for two soil types because the hydraulic properties of the soil strongly influence the relation between PE and E_a.

An important parameter for these simulations is the extinction depth. The extinction depth represents the groundwater table depth at which phreatic evaporation would approximate zero (Shah et al., 2007). The extinction depth of sand was set to be 0.5 m (Ma et al., 2019), and to 3.35 m for silty clay. This value is based on Shah et al. (2007). The models are run until steady-state conditions are reached for fixed water table depths of 0.1, 0.25, 0.5 and 0.75 m in sandy soils, 0.5, 1, 1.5, 2, 3, 4 m for silty clay. The fixed water tables are maintained through a constant head boundary.

HGS is based on the Richards equation which simulates flow in the unsaturated zone. The Richards equations relates fluxes to differences in hydraulic heads in the unsaturated zone. Capillary rise and infiltration processes are driven by head differences, and are thus directly simulated by HGS. The relation between saturation, pressure and hydraulic conductivity is parametrized using the van Genuchten approach (van Genuchten, 1980). Hydraulic properties from fine sand are taken from measurements, hydraulic properties for silty clay are based on Carsel and Parrish (1988). The saturated water content θ_s corresponds to the porosity. An overview of the soil hydraulic parameters is shown in Table 2.

HGS uses PE as an upper boundary condition, and calculates E_a as a function of soil moisture content (Therrien et al., 2010):

$$\begin{aligned} E_a &= \alpha^* \cdot (PE) EDF \\ \alpha^* &= \begin{cases} 1 & \theta > \theta_{e1} \\ \frac{\theta - \theta_{e2}}{\theta_{e1} - \theta_{e2}} & \theta_{e2} \leqslant \theta \leqslant \theta_{e1} \\ 0 & \theta < \theta_{e2} \end{cases} \end{aligned} \tag{15}$$

α^* is the wetness condition of the subsurface, determined by soil moisture content, EDF is the evaporation distribution function (a constant, quadratic and a cubic decay function can be used). We used a quadratic function in this study. Above θ_{e1}, evaporation is not limited by

Table 2
Soil hydraulic parameters used for calculating E_a.

Parameters	Sand	Silty Clay
Extinction Depth (m)	0.50	3.35
α (1/m)	3.40	0.5
n	2.75	1.09
K (m/s)	$9.26{\cdot}10^{(-5)}$	$5.56{\cdot}10^{(-8)}$
θ_s	0.38	0.36
θ_{e1}	0.95	0.95
θ_r	0.02	0.07
θ_{e2}	0.20	0.20

water availability in the soil, below θ_{e2} the actual evaporation is zero. θ is the actual soil moisture content calculated with the Richards equation. An additional condition for evaporation to occur is related to the pressure heads in the unsaturated zone. If the pressure head drops below a certain threshold (e.g. 1 m) no evaporation occurs.

Vertical discretization was sufficiently high (1 cm) to avoid numerical problems related to solving the Richards equation.

3. Results

3.1. Meteorological data and lysimeter measurements

3.1.1. Meteorology

Meteorological data from 2005 to 2020 (15 years) from Jinghe National Meteorological Station (a few kilometers away from our experiment site), are shown in Fig. 3. The yearly cycles of the average temperature and pan evaporation are plotted in Fig. 3a. The average monthly rainfall and sunshine duration are displayed in Fig. 3b. The hottest period of the year is between the beginning of July and the middle of August, with a mean temperature of 27.7 °C.

Based on the statistics over the period 2005–2020, evaporation during summer represents 38% of the evaporation of the whole year. Fig. 4 shows that summer temperatures in 2016 were higher than the long term average, with a mean value of 29.3 °C. Historically, rainfall is concentrated in August (Fig. 3b, average monthly precipitation ~87 mm), with less sunshine during that month (192 h). In 2016 the August was drier (50 mm precipitation) and sunnier (290 h sun). The period of August 11 until August 17 was the hottest period in 2016. The meteorological conditions of our experimental period are closely following the multi-annual characteristics in summer. Our selected period is therefore representative for warm, dry periods in summer with a high evaporative demand for the Guanzhong Basin.

Fig. 5 shows the time series and average diurnal cycles for the different meteorological variables in this period. This figure illustrates the typical daily cycles with maximum values for wind speed, air temperature and incoming radiation terms in the afternoon, and minimal daily values of relative humidity and vapor pressure.

The average wind speed reaches a maximum in the afternoon. In general, wind speed is relatively low in the Guanzhong Basin. Air temperature is fluctuating between 26 and 39 °C during this week with a mean value of 32.3 °C. Relative humidity varies between 33 and 75% with a mean value of 53%. Vapor pressure varies between 2 and 2.8 kPa. Incoming radiation is the energy input for evaporation, incoming short wave radiation varies between −3 and 900 W/m^2 and incoming longwave radiation is around 450 W/m^2. The maximum value of radiation occurred around 12:50 (Beijing Time), as it is the local midday time in summer.

3.1.2. Temperature profiles in the lysimeter columns

Fig. 6 shows the half-hourly vertical temperature variation for saturated fine sand (T_s) and water (T_w) on the basis of measurements at 3, 5, 10, 20, 30 and 50 cm depth. T_s and T_w roughly follow a sine function (Fig. 6 C) related to the net radiation balance.

The variations of T_s with depth show considerable differences in time. The timing of the maximum and minimum values for T_s, and corresponding amplitudes at different depths are shown in Table 3. The amplitude of T_s is smaller with increasing depth. This is related to the fact that incoming radiation cannot penetrate soil and heat the soil surface only. The downward heat transport is delayed because of heat storage and the relatively slow heat conduction in soil. These dynamics are highlighted in Fig. 6A. The slope of T_s along the vertical soil profile is indicated by the angle β. It is a proxy for the temperature transmission time in the vertical direction, slower transmission associated with larger angles.

On the other hand, T_w is quite uniform over depth. The temporal evolution of the vertical gradient of T_w indicates that the water column is well mixed (the black line in Fig. 6 B, the angle of the gradient along the vertical profile β is 0). This can be explained as follows: (1) Water has a bigger heat capacity than soil, and daily temperature variations are more strongly buffered than in soil. (2) Short wave radiation can penetrate deeper in the water column thus directly heating a larger vertical column than for soil. (3) Moreover, vertical mixing might be increased through wind which is not the case for the soil column.

3.2. Potential evaporation

Fig. 7 shows the measured daily average temperatures and PE rates from August 1st to 26th. The differences in PE between fine sand and water are more obvious during “hot days” (August 11th-17th), detailed analyses were made for these seven consecutive days.

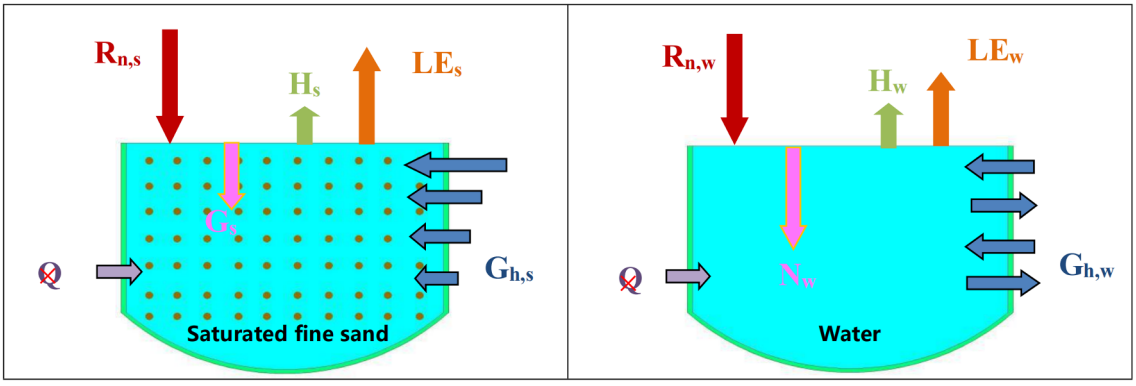

Fig. 2. Schematic diagram of the energy balance for saturated fine sand (left) and the water column (right): R_n is the net radiation, G_s/N_w is soil heat flux/ water heat storage, H is the sensible heat flux, LE is latent heat flux for evaporation, G_h is horizontal heat flux, Q is the energy associated with incoming water from the Markov bottle, red cross means it is neglected in this study. (For interpretation of the references to colour in this figure legend, the reader is referred to the web version of this article.)

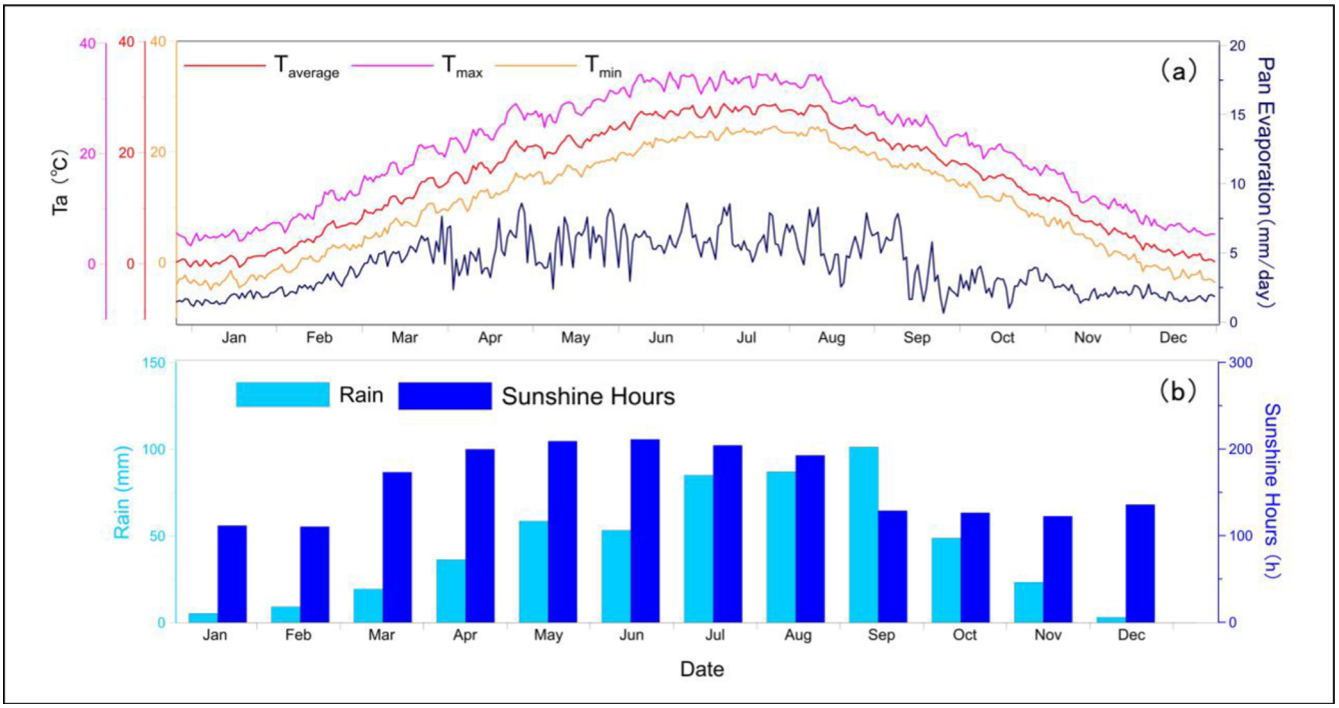

Fig. 3. Average climatic variables for the period 2005–2020 at Jinghe National Meteorological Station. (a) daily maximum, average and minimum temperatures and pan evaporation. (b) monthly rainfall amount and sunshine duration.

3.2.1. Diurnal PE dynamics

Fig. 8 shows the diurnal time series of PE_s and PE_w, together with the average diurnal cycles. The time series of PE_s and PE_w were different in terms of absolute values and temporal dynamics.

For PE_s, ~78% of the daily evaporation took place between sunrise and sunset (~5:30–19:30), the remaining 22% evaporate after sunset. On the other hand, for the water lysimeter, nighttime evaporation is ~5% larger than daytime evaporation. As Fig. 8c illustrates, between 9:00 and 17:30 $PE_s > PE_w$, but during night time $PE_s < PE_w$. The peak value for PE_s was larger than for PE_w, and the average daily sum of PE_s was ~21% higher than for PE_w.

The peak value of PE_s was measured in the afternoon (~14:00–16:00), while PE_w reached its maximum later in the evening (~20:00–22:00). The minimum of PE_s occurred during the night while for PE_w it was around noon. The peak value of PE_w is lagging ~6 h behind the one for PE_s. Also, PE_s and PE_w were lagging behind the

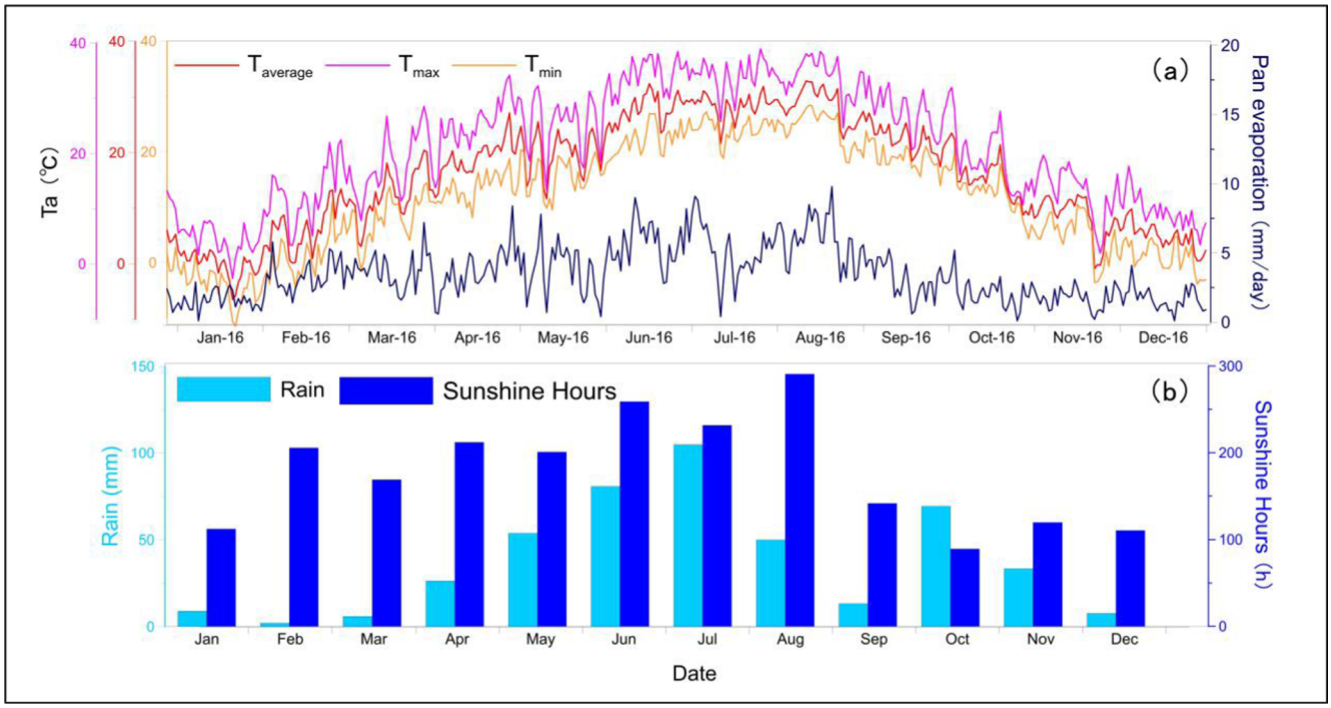

Fig. 4. Climatic variables for the year 2016 at Jinghe National Meteorological Station. (a) daily maximum, average and minimum temperatures and pan evaporation. (b) monthly rainfall amount and sunshine duration.

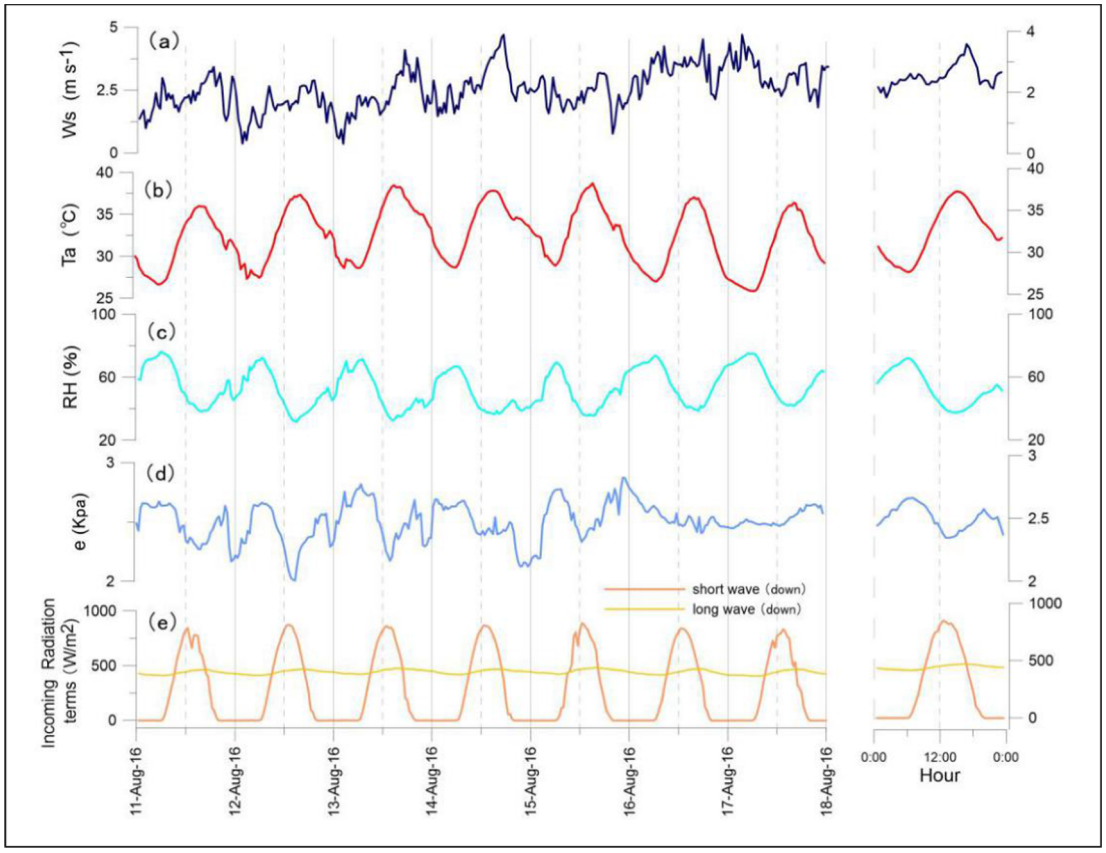

Fig. 5. Time series of (micro)meteorological variables (left) and average diurnal cycles (right): (a) WS (wind speed); (b) T_a (air temperature); (c) RH (relative humidity); (d) e (vapor pressure); (e) Incoming radiation terms (long and short wave radiation).

diurnal cycles of meteorological variables (ME), but for PE_w this lag was much larger than for PE_s. Linear correlation analysis was used to determine this specific "lag time".

In order to assess the lag time, a simple time-shift was introduced and the linear correlation coefficients between PE and the meteorological variable were calculated. Tables 4 and 5 show that for time lag zero (t + 0), PE_s has a positive correlation with net radiation, air temperature and wind speed. Negative correlations are observed with humidity and vapour pressure. PE_w has a relatively strong positive correlation with wind speed, while for other variables, the correlation coefficients reach their maximum value for relatively large time lags of 4–6 h, illustrating that PE_w lags behind the meteorological variables. In summary, the diurnal cycle of PE_w lagged almost 4–5 h behind the one for PE_s during summer. This can be explained by energy balance considerations, as discussed in the next section.

3.3. Energy fluxes

3.3.1. Net radiation

Fig. 9 shows the diurnal variation of the calculated flux terms for the saturated fine sand and water columns in equation 12. Fig. 9a shows the net radiation R_n, which is the energy input for the fine sand and water columns. Net radiation was slightly negative during nighttime and increased after sunrise (~7:00), reaching a maximum around 13:00 (water: 720 W/m^2, saturated fine sand: 540 W/m^2), and decreasing afterwards, again turning into negative in the beginning of the evening around sunset. The green curve (Fig. 9a right) represents the difference between $R_{n,w}$ and $R_{n,s}$, the value is positive during the daytime, as the albedo of water is lower than for fine sand.

3.3.2. Heat flux/storage

G_s (for fine sand) and N_w (for water) represent the energy variation related to heat storage inside the column system (Fig. 9b). The curves of G_s and N_w have different shapes, with N_w having a much more

Table 3
The timing of maximum and minimum value of T_s and amplitudes at different depths.

Textures	Depth (cm)	Maximum temperature		Minimum temperature		Amplitude (°C)
		Value (°C)	Point in time	Value (°C)	Point in time	
Saturated fine sand	3	36.4	14:30–15:30	26.5	6:00	9.9
	5	34.8	16:00	28.4	7:00	6.4
	10	33.8	16:00–17:00	28.4	7:00–8:00	5.4
	20	31.7	19:00	29.3	9:00	2.4
	30	31.0	21:00–22:00	29.7	12:00	1.3
	50	30.1	23:00	29.7	14:00	0.4

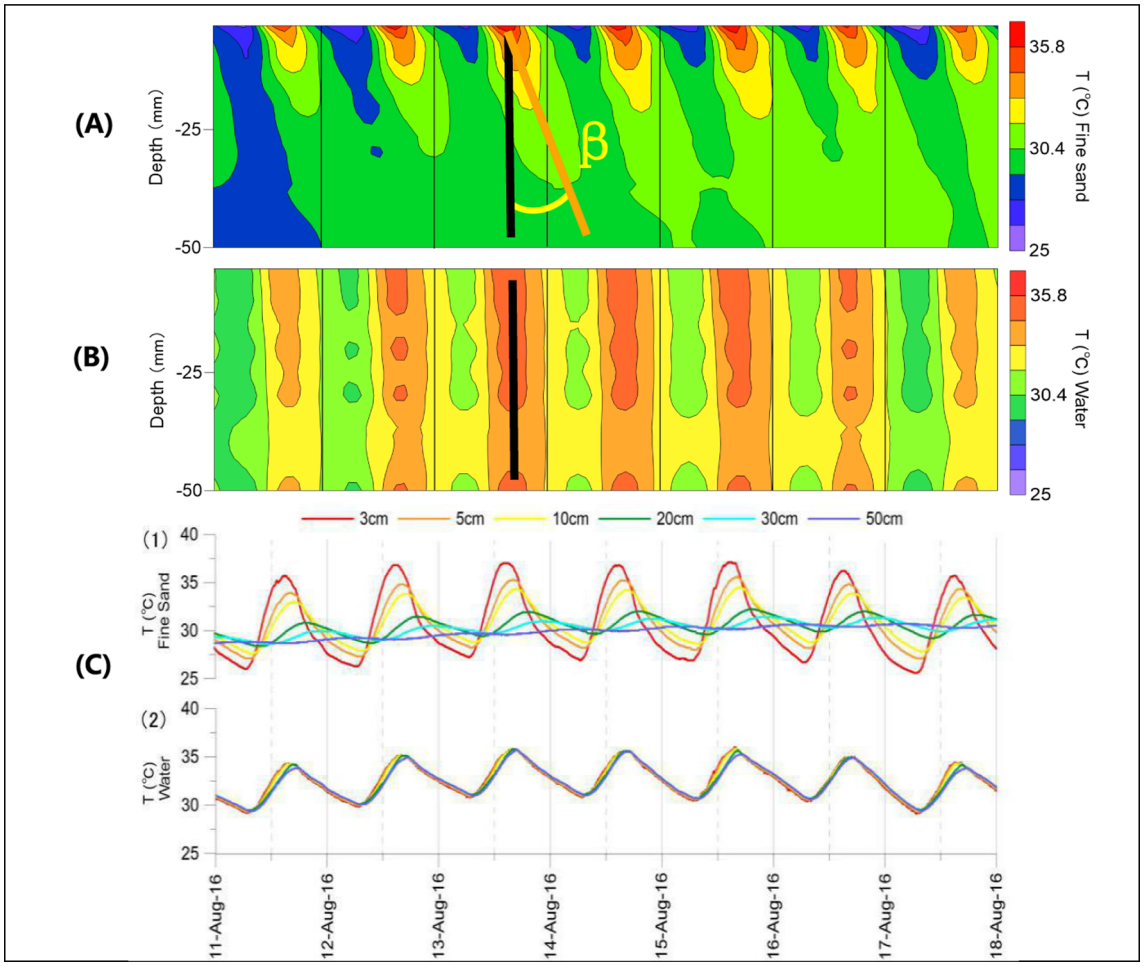

Fig. 6. (A) Lysimeter soil column temperature variations for the measurement period of the 11th-17th August 2016. β is the angle of the temperature gradient along the vertical soil profile; (B) Water column temperature variations, the black line is the gradient along the vertical water profile; (C) Temperature distribution as a function of depth and time for saturated fine sand (1) and water (2).

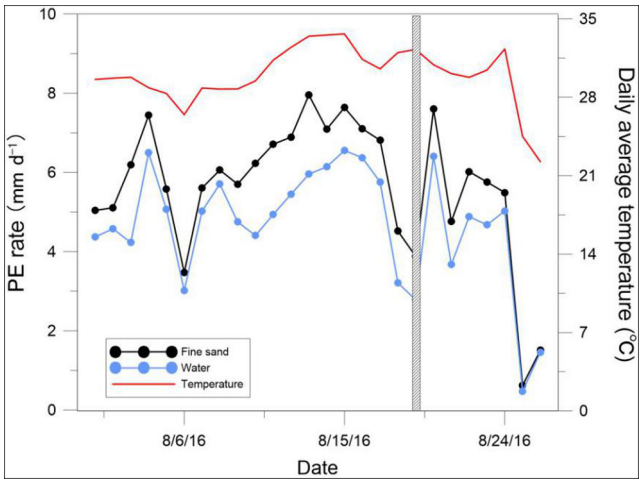

Fig. 7. Measured daily average temperatures and measured daily, cumulative PE for the lysimeter columns filled with saturated fine sand and water. No data could be recorded on the 19th, indicated through the vertical gray bar in the figure.

pronounced daily amplitude. Both N_w and G_s are negative during the night, and N_w has more negative values than G_s (-250 W/m^2 resp. -50 W/m^2 on average; -340 W/m^2 resp. -64 W/m^2 as minimum values). The time series for G_s and N_w reach positive values during day time (8:00–17:30). The green time series in the right of Fig. 9b displays the diurnal cycle of the average difference between N_w and G_s. During daytime the water column stores more heat than saturated bare soil (the maximum difference is around 540 W/m^2), and releases more energy during the night. This is related to the increased heat capacity of water compared to the soil.

3.3.3. Horizontal heat flux

Horizontal energy exchange between the lysimeter and the surroundings $G_{h,s}$ (or water $G_{h,w}$) is important for energy closure. The results are shown in Fig. 9c. The two curves show a similar trend. $G_{h,s}$ is positive from 18:00–13:00 as heat is transferred from the surroundings into saturated fine sand, reaching the maximum value (~110 W/m^2) before dawn, and is negative in the afternoon. $G_{h,w}$ is negative most of the time, except from 2:30–10:00, as heat is transferred from the water column to the surroundings. In general, the lysimeter columns are absorbing heat during the night and releasing heat at day.

3.3.4. Sensible heat flux

The sensible heat flux H represents the turbulent exchange of sensible heat at the interface of the land and the atmosphere. Results are shown in Fig. 9d. H_w is negative from 10:30–20:30, as heat is transferred from the overlying air into the water, and positive from 21:30–10:00 as water is releasing sensible heat to the air, the net sum of H is close to zero. In general, during the summer months, H_w is close to zero (Finch, 2001).

H_s is negative most of the time, except around noon. In this

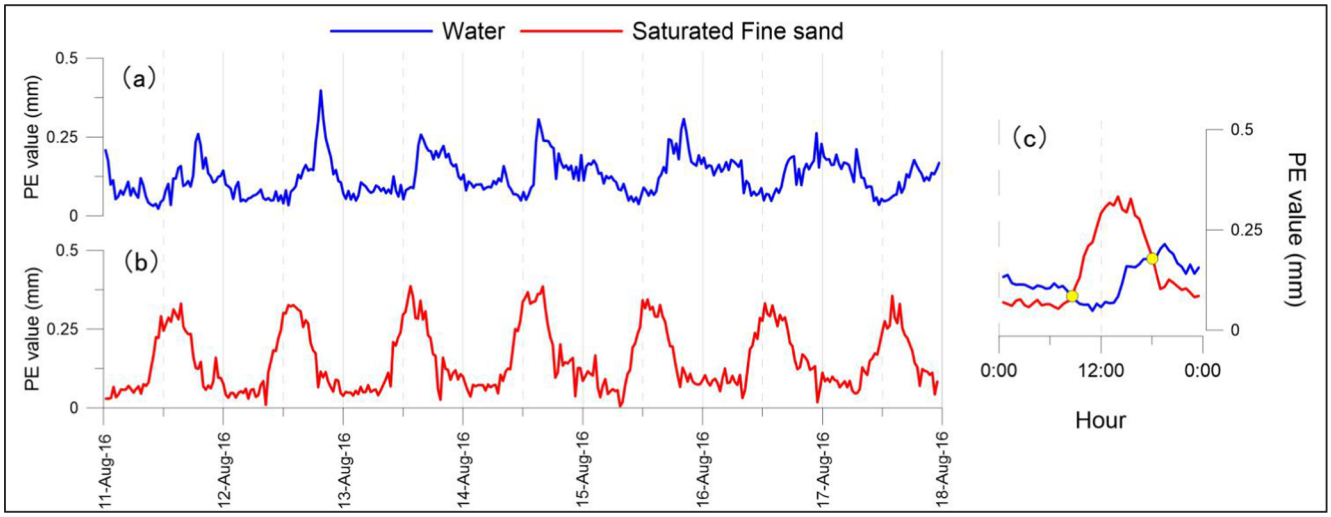

Fig. 8. Diurnal variations (on the basis of half hourly data): (a)PE_w; (b) PE_s; (c) the average diurnal cycles of PE_w and PE_s.

Table 4
Linear correlation coefficients between PE_s and different meteorological variables (ME) for different time lags: WS (wind speed); T_a (air temperature); RH (relative humidity); e (vapor pressure); R_n (net radiation).

Evaporation surface	PE_s						
ME / Time lag (hours)	t + 0	t + 0.5	t + 1	t + 1.5	t + 2	t + 2.5	t + 3
WS	**0.26**	0.23	0.17	0.13	0.11	0.09	0.08
T_a	0.74	**0.77**	0.59	0.49	0.39	0.27	0.15
RH	**−0.71**	−0.65	−0.57	−0.48	−0.37	−0.25	−0.13
e	**−0.44**	−0.38	−0.32	−0.26	−0.18	−0.08	0.02
R_n	0.87	0.92	**0.94**	**0.94**	0.91	0.86	0.80

experimental setup, we have a so-called “oasis effect” which occurs primarily in summer. It is related to the fact that the lysimeter is always saturated and shows a strong evaporation, whereas the surroundings have low soil moisture content. Net radiation is therefore mainly used for sensible heat flux (Hao et al., 2016). The evaporation over the lysimeter is enhanced by the high air temperatures in the surrounding of the lysimeter so that the soil surface temperature is smaller than the measured air temperature ($T_s - T_a < 0$). The oasis effect induces lateral transfer of sensible heat towards the lysimeter causing lower H and larger LE than in normal situations. Therefore, the sensible heat flux above the lysimeter is small and almost all available energy is used for evaporation and heat storage in sand and water columns.

During summer, the absolute value of H above a well-watered surface is significantly smaller than the latent heat flux. A range of studies found that H can be negligible compared with net radiation or latent heat flux (Tanner and Pelton, 1960; Katul and Parlange, 1992; Finch, 2001; Gallego-Elvira et al., 2011).

3.3.5. Latent heat flux for both lysimeters

Fig. 10 shows the measured and calculated time series of latent heat for evaporation (LE_s and LE_w) according to the energy balance method, the Penman-Monteith (PM) and Priestly-Taylor (PT) equations based on half-hourly data.

Table 6 shows the daily average value of PE calculated by PM, PT and the energy balance equations. In order to compare the different approaches, different evaluation statistics were calculated: the coefficient of determination (R^2), root mean squared error (RMSE), mean absolute error (MAE) and mean bias error (MBE) between calculated and measured LE for seven days and for the average diurnal cycles. Table 7 shows the evaluation statistics.

All three methods resulted in a relatively good estimation of PE. The estimation of LE_s corresponds better to the measurements than the estimation of LE_w (with bigger R^2). Based on the different statistical measures, the quality of the estimated values of LE by the three different methods was similar, with slightly better performance of the energy balance method for the soil columns (lowest RMSE and MAE among methods), while for the water column none of the methods clearly outperforms another method (PM provides the best results in terms of RMSE and MAE, but energy balance in terms of R^2 and PT in terms of MBE).

3.4. Calculation of actual evaporation E_a using numerical models

Fig. 11 shows the results of the numerical simulations. $E_{a,s}$ is the actual evaporation rate calculated from measured PE_s. $E_{a,w}$ is the actual evaporation rate calculated from measured PE_w, with their differences ΔE_a ($= E_{a,s} - E_{a,w}$). The relative difference between $E_{a,s}$ and $E_{a,w}$ calculated by HGS were highlighted as RD (Fig. 11 b, d):

$$RD = \left(\frac{E_{a,w}}{E_{a,s}} - 1\right) \cdot 100\% \quad (16)$$

Table 5
Linear correlation coefficients between PE_w and different meteorological variables (ME) for different time lags.

Evaporation surface	PE_w										
ME / Time lag (hours)	t + 0	…	t + 2	…	t + 4	t + 4.5	t + 5	t + 5.5	t + 6	t + 6.5	t + 7	t + 7.5
WS	**0.41**		0.37		0.22	0.18	0.14	0.14	0.10	0.08	0.06	0.04
T_a	0.26		0.54		**0.65**	**0.65**	0.63	0.60	0.52	0.45	0.39	0.31
RH	−0.23		−0.50		**−0.62**	−0.62	−0.60	−0.57	−0.48	−0.41	−0.34	−0.26
e	−0.07		−0.28		**−0.36**	−0.33	−0.30	−0.26	−0.16	−0.08	−0.02	0.06
R_n	−0.36		0.03		0.43	0.50	0.56	0.60	**0.64**	0.63	0.61	0.58

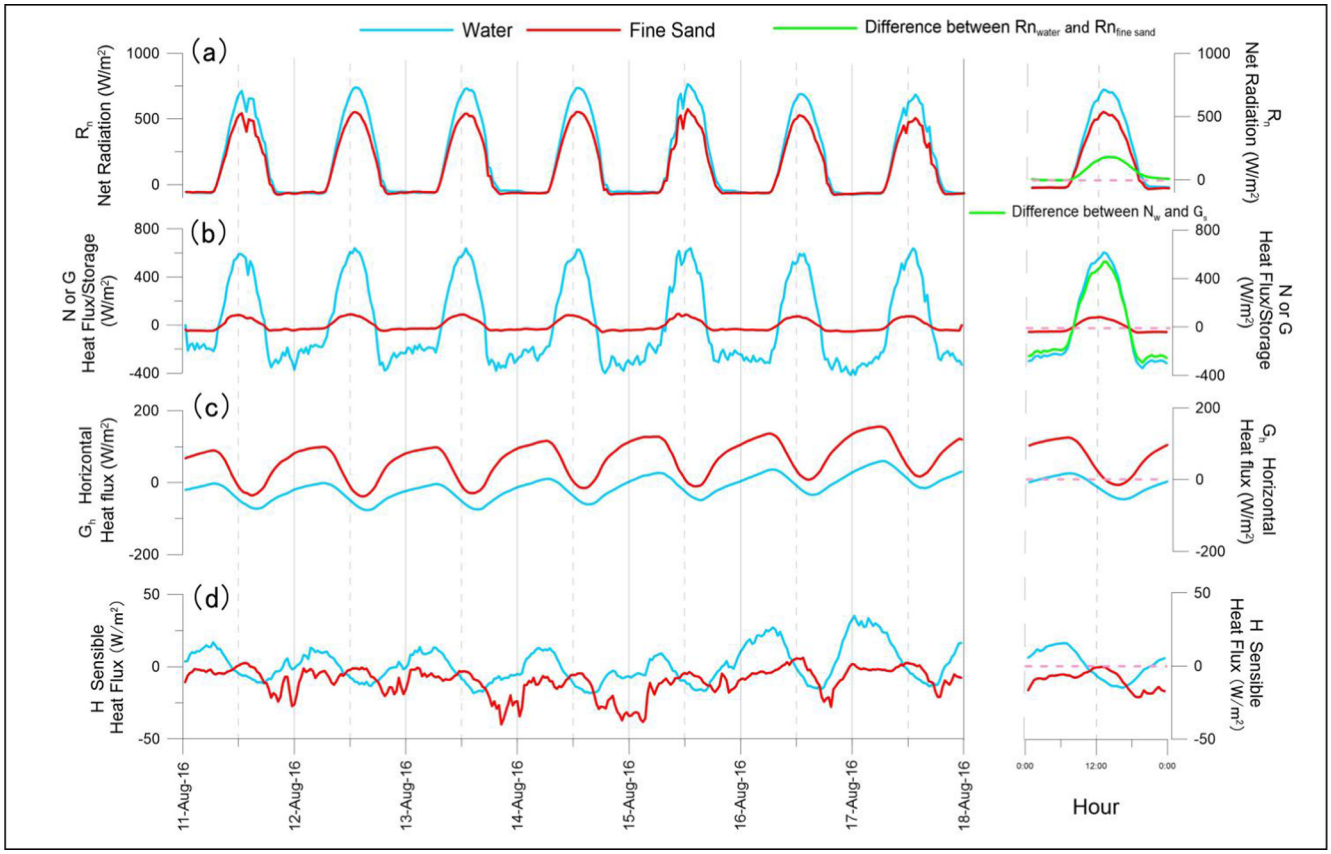

Fig. 9. Time series of calculated components of the energy balance (on the basis of half hourly data) including the average diurnal cycle on the right: (a) Net radiation; (b) Heat flux or storage; (c) Horizontal heat flux; (d) Sensible heat flux.

Differences over 17% can occur for the estimates of E_a (Fig. 11). Fig. 11 (a, c) also illustrates that both $E_{a,s}$ and $E_{a,w}$, along with their differences ΔE_a approximate zero with the increase of the water table depth. The depth where evaporation drops to zero can be slightly larger than the extinction depth because the imposed extinction depth has not been established jointly with the soil-evaporation parameters. For sandy soil, the absolute value of relative differences were up to 17.5% (Fig. 11 b). For silty clay, relative differences decreased with the increase of water table depth (Fig. 11 d).

4. Discussion

4.1. Experimental setup and data analysis

The experimental setup developed in this study allows for a unique comparison between evaporation dynamics over an open water surface as well as saturated bare soil with a very high temporal resolution. The employed Markov-bottle approach proved suitable in this experimental setup. The size of the lysimeters was relatively large (1.0 m^2 each) and deep (0.7 m each). To the best of our knowledge, this is the first time such a detailed study on the dynamics of potential evaporation has been carried for a warm temperate semi-arid continental monsoon climate region.

A complication of the study was the horizontal heat-exchange between the lysimeter and the surrounding soil. Insulating the lysimeters could reduce heat exchange with the surrounding soil, but even with additional insulation horizontal heat exchange will not be zero. We have considered this effect by estimating horizontal heat exchange using average values of the vertical temperatures in the lysimeters. This is straightforward for the water column as vertically no relevant temperature differences were observed. For soil it is more complicated. Our suggested depth-weighted approach constitutes a simple calibration procedure (by manually modifying φ in equation 9) to close the energy balance under consideration of horizontal heat exchange. Clearly, this is a simplification of the underlying physics. A more complete analysis, however, would require a spatially distributed numerical model of the energy fluxes which was beyond the scope of this paper.

The study focused on a relatively short time span, but our selected period is representative for warm, dry periods in summer with a high evaporative demand. In addition to analyzing daily dynamics, studying long-term seasonal dynamics would certainly also be of interest but was also not the focus of this study. In summary, the chosen experimental setup and the subsequent treatment of the data were considered to be of sufficient accuracy for the subsequent analysis.

4.2. Potential evaporation over open water and saturated bare soil

The comparison between the two lysimeters revealed differences in both the absolute value as well as the temporal dynamics. For the analyzed period, differences up to 21% between the two average PE rates were observed. The diurnal cycle of PE_w lagged almost 4–5 h behind the one for PE_s during summer. This can be explained by energy balance considerations. These differences show the importance of the composition of the ground for estimating potential evaporation rates. These two findings have a range of implications. For example, precision agriculture requires accurate temporal estimates of evaporation dynamics of the soil to estimate hourly irrigation rates. The differences in the absolute values are important for all approaches which estimate actual evaporation based on potential evaporation.

The following physical properties differ between the saturated bare soil and water columns: (1) The surface albedo, (2) The thermal properties, including the differences in heat capacity, thermal

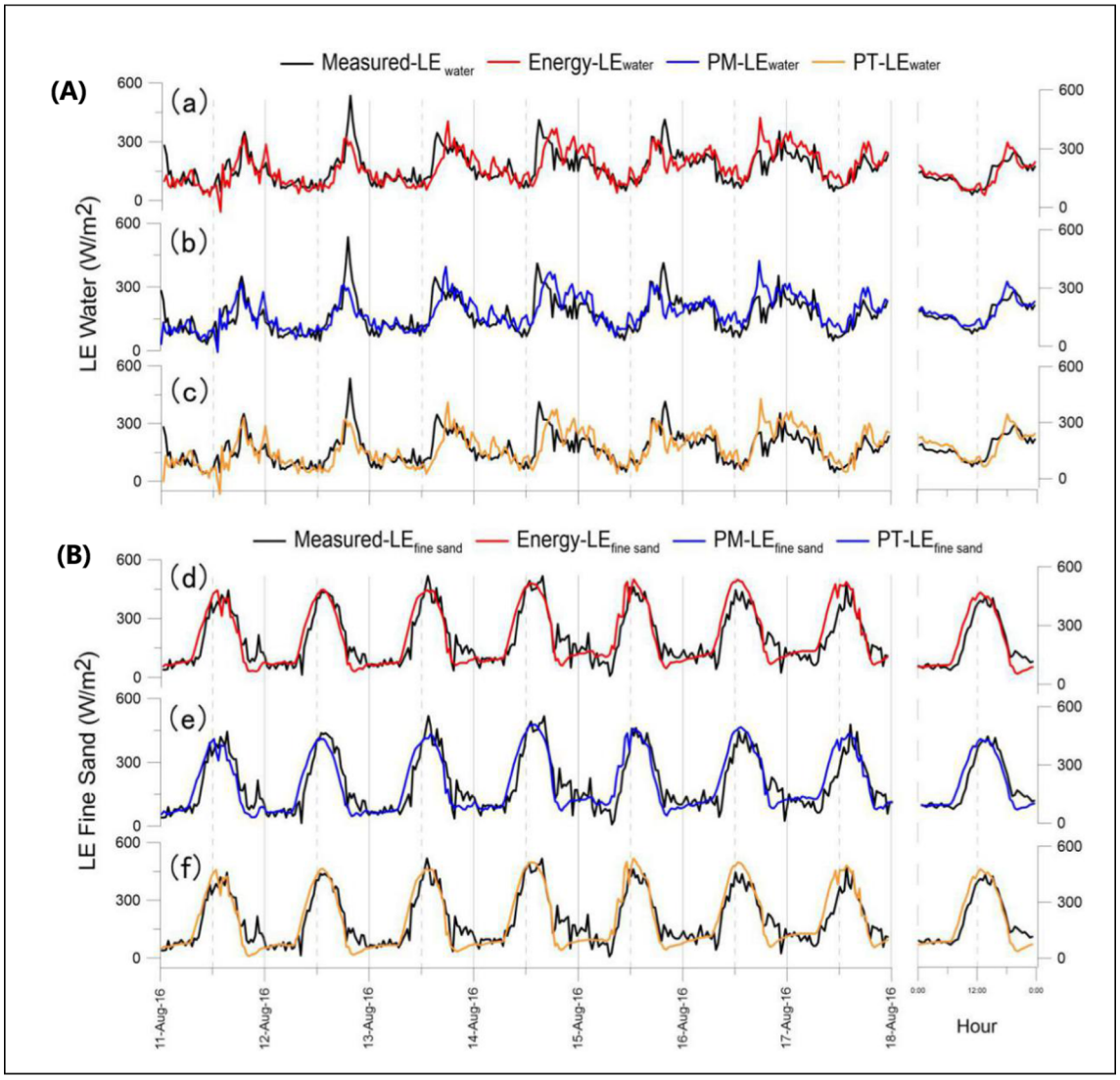

Fig. 10. Measured (black curve) and calculated latent heat flux for the lysimeter water column (A) and the lysimeter sand column (B) according to the energy balance (a,d—red curve), PM (b,e—blue curve) and PT (c,f—orange curve) equations. The average diurnal cycles are shown on the right. (For interpretation of the references to colour in this figure legend, the reader is referred to the web version of this article.)

Table 6
Daily average value of calculated PE (by PM, PT and the energy balance method) for the water and soil columns and differences with measured PE.

	PE_w (mm/d)	Difference (mm/d)	PE_s (mm/d)	Difference (mm/d)
Measured	5.88	–	7.09	–
PM	6.31	+0.43	7.13	+0.04
PT	6.09	+0.21	7.08	−0.01
Energy Balance	6.07	+0.19	7.35	+0.26

conductance and the depth of energy adsorption.

In our case the albedo of the soil is larger than the albedo of water (as shown in Fig. 9a), resulting in a decreased amount of absorbed energy. Note that this does not necessarily mean that the latent heat flux for evaporation is smaller for soil, because the re-distribution of energy is also significantly affected by the physical properties of the underlying material. Our analysis identified significant differences in the soil heat flux related to vertical differences of temperature, and the heat storage in the water. Fig. 12 shows the temperature data used to calculate N_w and G_s ($G_0 + \Delta S$). Although the vertical temperature gradient is smaller for water than for soil, N_w is much larger than G_s (shown in Fig. 9b), leaving less energy for evaporation, which is caused by the differences in thermal properties.

The difference in vertical temperature gradients between the soil and water columns, which influence G_s and N_w, can be explained. During the day, for saturated fine sand, net radiation can only heats a thin surface layer of the soil column, and heat slowly diffuses downwards, resulting in a relatively small value for the soil heat flux G_s. Therefore, a more important fraction of the net radiation is available for evaporation. For water, on the other hand $G_{h,w} + R_{n,w}$ is mainly used to heat water. We found that: $G_{h,w} + R_{n,w} - N_w < G_{h,s} + R_{n,s} - G_s$, so less energy is available for latent heat flux, even though R_n for the water column is higher than for the fine sand column.

During the night, besides $G_{h,s}$, both R_n, G_s and N_w are negative, and N_w is more negative than G_s, thus $G_{h,w} + R_{n,w} - N_w > G_{h,s} + R_{n,s} - G_s$, water releases energy stored during the daytime for evaporation, so that water has a bigger evaporation rate than saturated fine sand at night.

4.3. Performance of approaches to estimate PE

4.3.1. Energy balance method and Priestly-Taylor equations

Given that the Priestly-Taylor and the energy balance resulted in nearly identical diurnal curves, the discussion of the energy balance

Table 7
Evaluation Statistics: R^2, RMSE, MAE and MBE between calculated and measured latent heat fluxes (LE) for the saturated fine sand column and the water column, by PM, PT and the energy balance equation for seven consecutive days and average diurnal cycles.

Evaluation statistics	Method	7 Days		Average Diurnal cycles	
		LE_w	LE_s	LE_w	LE_s
R^2	PM	0.40	0.78	0.71	0.82
	P-T	0.45	0.82	0.71	0.88
	Energy Balance	0.47	0.81	0.75	0.87
RMSE (W/m^2)	PM	62.72	76.91	30.62	56.01
	P-T	69.09	67.59	37.13	55.64
	Energy Balance	65.72	61.42	32.70	43.76
MAE (W/m^2)	PM	45.06	51.54	23.38	42.00
	P-T	49.47	51.40	28.85	43.10
	Energy Balance	47.52	47.17	24.89	34.58
MBE (W/m^2)	PM	+12.09	+1.31	+12.31	+1.76
	P-T	+4.61	−0.15	+5.84	−0.32
	Energy Balance	+5.57	+6.86	+5.36	+6.68

likewise applies to the PT method.

The results calculated from the energy balance equation are discussed by introducing the energy balance ratio (EBR): $(LE_{measured} + H)/(G_h + R_n - G_s \text{ or } N_w)$ is equal to 1 if the energy budget is closed. If EBR > 1, calculated LE is underestimated compared to $LE_{measured}$. If EBR < 1, calculated LE is overestimated.

For water, the energy balance cannot be closed satisfactorily. LE_w is significantly underestimated from 13:00–15:30 (EBR > 1) and overestimated from 17:30–19:00 (EBR < 1). The imbalance from 13:00–15:30 can be explained with errors associated with the overestimation of heat storage N_w. These errors are related to the vertical temperature variations. As can be seen in Fig. 6, some stratification took place. However, the vertical discretization to calculate changes in heat storage might have been too coarse to capture these variations adequatly. The second imbalance occurred in the evening. This might be related to the high wind speed and turbulence in the evening, which leads to ripples in the water column, potentially causing measurement errors (Arnon et al., 2014; Lensky et al., 2018).

For saturated fine sand, the energy balance closure could be achieved during daytime. However, an imbalance existed between 8:00–11:00 (EBR < 1) and 19:30–23:00 (EBR > 1). The first imbalance occurred in the morning, the calculation overestimates LE_s. There appears to be a certain time-lag between available energy and the onset of

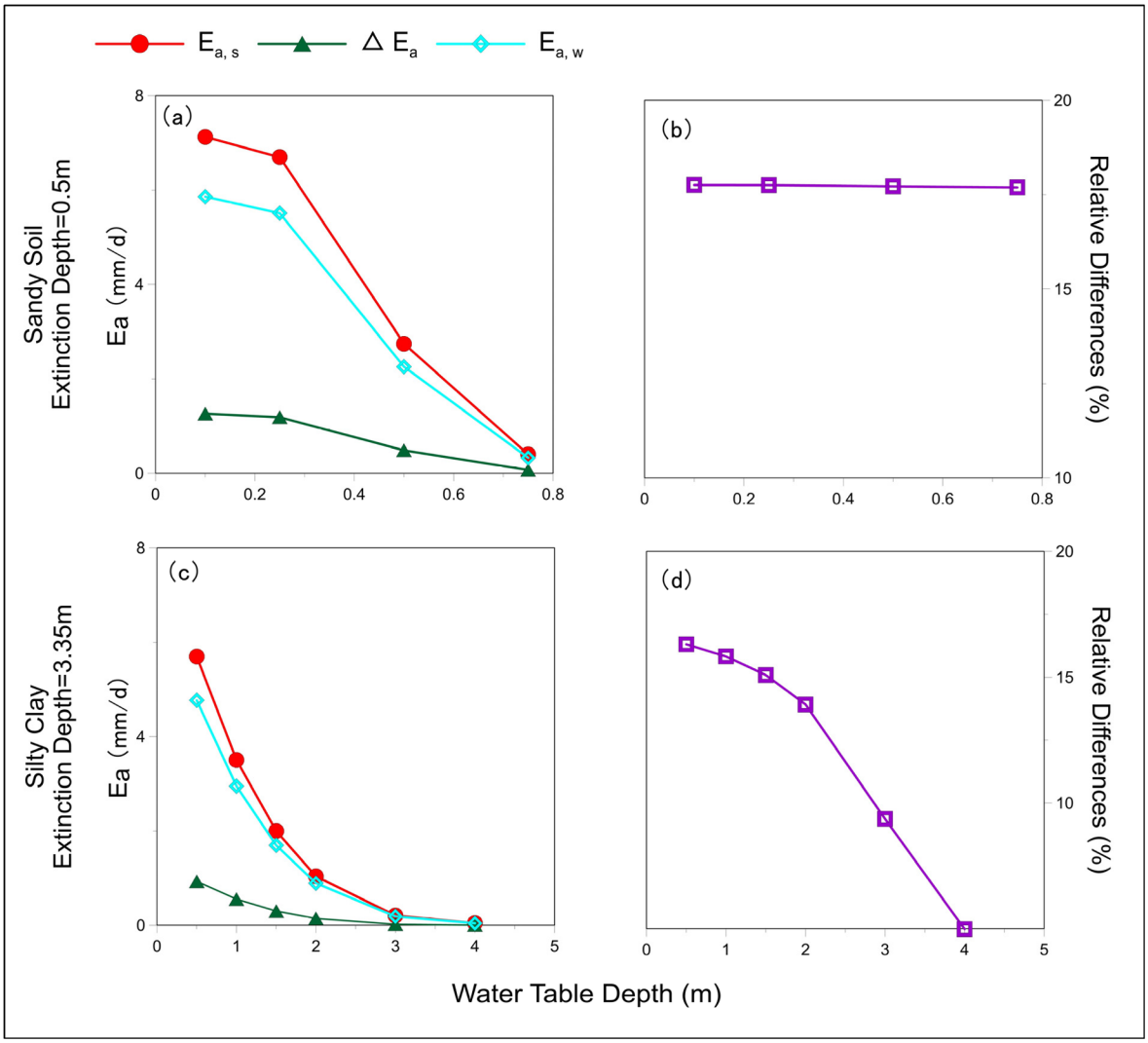

Fig. 11. Influence of different PE on calculating E_a by the hydrological model HGS, for different water table depths. (a), (c): $E_{a,s}$ is the actual evaporation rate calculated from measured PE_s (red curve); $E_{a,w}$ is the actual evaporation rate calculated from measured PE_w (blue curve); $E_{a,s}$–$E_{a,w}$, represented as ΔE_a (green curve); (b), (d): Relative differences between $E_{a,s}$ and $E_{a,w}$ (purple curve). (For interpretation of the references to colour in this figure legend, the reader is referred to the web version of this article.)

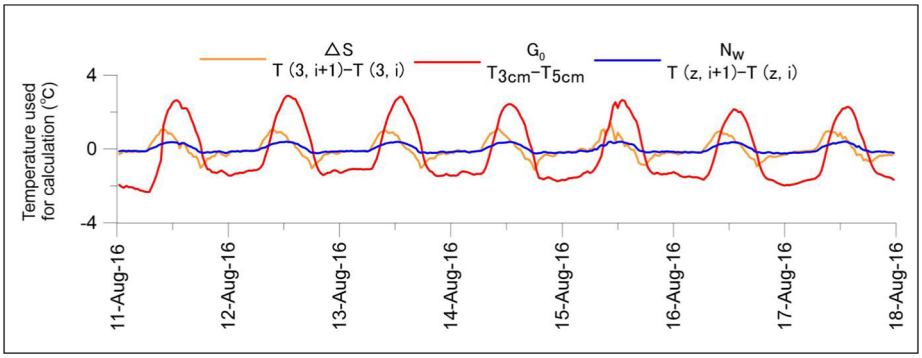

Fig. 12. Half-hourly temperature time series used to calculate water heat storage N_w (blue); saturated fine sand heat flux G_0 (red), and heat storage in the top sand layer ΔS (orange). (For interpretation of the references to colour in this figure legend, the reader is referred to the web version of this article.)

evaporation. The second imbalance occurred after sunset, when LE_s was underestimated. This might be related to the relative importance of the soil heat flux at night. Already small biases of G_0 will play a major role in the estimation of the latent heat flux at night. The inability to close the energy balance during these periods can, therefore, be related to inaccuracies in estimating G_0 (An et al., 2016). Errors on G_s (includes ground heat flux G_0 and heat storage ΔS) are, as suggested by (Foken, 2008), probably the most important source of error affecting the energy balance in most conditions.

Although during some periods the energy balance could not be closed for both open water and fine sand columns, it did not significantly affect the reliability of this study. Balance closure is difficult to achieve, and the improvement of theory and observation methods in the future should allow for reducing this error.

4.3.2. Penman-Monteith equation

The application of the PM equation on the fine sand and water columns shows a satisfactory correlation with measured data on a daily time-scale. Fig. 13 shows the time series for calculated aerodynamic resistance r_a, the aerodynamic term for evaporation LE_{aero} (equation 13) and parameter α_{PT} based on the Penman-Monteith equation ($\alpha_{PT} = LE_{PM}/LE_{energy}$).

The values of r_a were inversely proportional to wind speed and LE_{aero} (Mahrt and Ek, 1984; Choudhury et al., 1986; Viney, 1991; Yang et al., 2001; Liu et al., 2007), its influence on the evaporation rate mainly depends on wind speed and the surface roughness. During the research period, wind speed was higher in the evenings, resulting in smaller r_a and higher LE_{aero} rates (Fig. 13 a,b,c) for both soil and water during the evening.

In the PT equation, $\alpha_{PT} = 1.26$ which impies that the LE_{aero} value is replaced with 0.26 ($\alpha_{PT} - 1$) times of LE_{energy}. As shown in Fig. 13 d, instead of a fixed value, actual α_{PT} varies over a large range. The contribution of LE_{aero} to total LE was different for the soil and water columns. For the saturated bare soil column, the available energy term "$G_{h,s} + R_{n,s} - G_s$" is bigger at day, so that the aerodynamic resistance contribution to LE_s is smaller at day and bigger in the evening. On the other hand, for the water column, the energy term is smaller around noon resulting in a larger contribution of the aerodynamic term.

Our results also suggest that the good performance of the three methods highly depends on accurate calculation of the energy balance terms, especially also the total heat flux or heat storage.

4.4. The effect of different PE on calculating E_a using numerical models

E_a was calculated by HGS for both sandy soil and silty clay, using measured PE_s and PE_w as input. Differences up to ~17.5% of the resulting E_a were observed. Given the dependency of PE on the surface properties, we propose to calculate PE in hydrological modelling studies for different surface types, instead of imposing one value of PE across the entire modelling domain.

The above-mentioned results are especially important for large-scale distributed hydrological models. An alternative is to employ land surface models where water and energy balances are solved in a coupled fashion. However, in many hydrological modelling studies this is not feasible, so that the PE-choice becomes of high importance. Further research will provide a more solid assessment based on larger time series.

5. Conclusions

Potential evaporation was measured during August 2016 for saturated fine sand (PE_s) and water (PE_w) columns, using lysimeters installed in the Guanzhong Basin, China. The experimental setup allowed for a very high temporal resolution of all measured quantities. This study, therefore, goes beyond previous assessments of potential evaporation. To the best of our knowledge it is also the first time these dynamics were studied in such detail for semi-arid climates. The measurement data were analyzed with the help of energy balance considerations and numerical calculations. The following conclusions can be drawn:

- The application of lysimeters as suggested in this study proved to be highly beneficial. It allowed to achieve an unprecedented temporal resolution on the dynamics of potential evaporation.
- Diurnal dynamics of PE_s and PE_w are significantly different, PE_s was higher than PE_w. PE_w was lagging 4–5 h behind PE_s. This has important implications for all applications where a high temporal resolution of evaporation estimates is required, for example for precision agriculture.
- All three methods employed to estimate PE performed well. The Penman-Monteith equation and the energy balance approach describe both the radiative and aerodynamic processes during day and night. From a theoretical point of view, it is based on a comprehensive description of the relevant processes. Nevertheless, the Priestly-Taylor approach performed approximately as good as the Penman-Monteith approach, in spite of the simplifications. The energy balance approach performed slightly better than the other approaches for the sand column. Note that these findings are specific to the climate conditions tested.
- The calculation of actual evaporation based on the potential evaporation is, not surprisingly, strongly influenced by the choice of calculating PE (saturated bare soil or water). We observed relative differences in actual evaporation up to 17.5%. If evaporation is calculated at the regional scale with a hydrological model, the estimation of PE has to carefully consider the different surface types, in addition to spatial and temporal variations of climatic data.

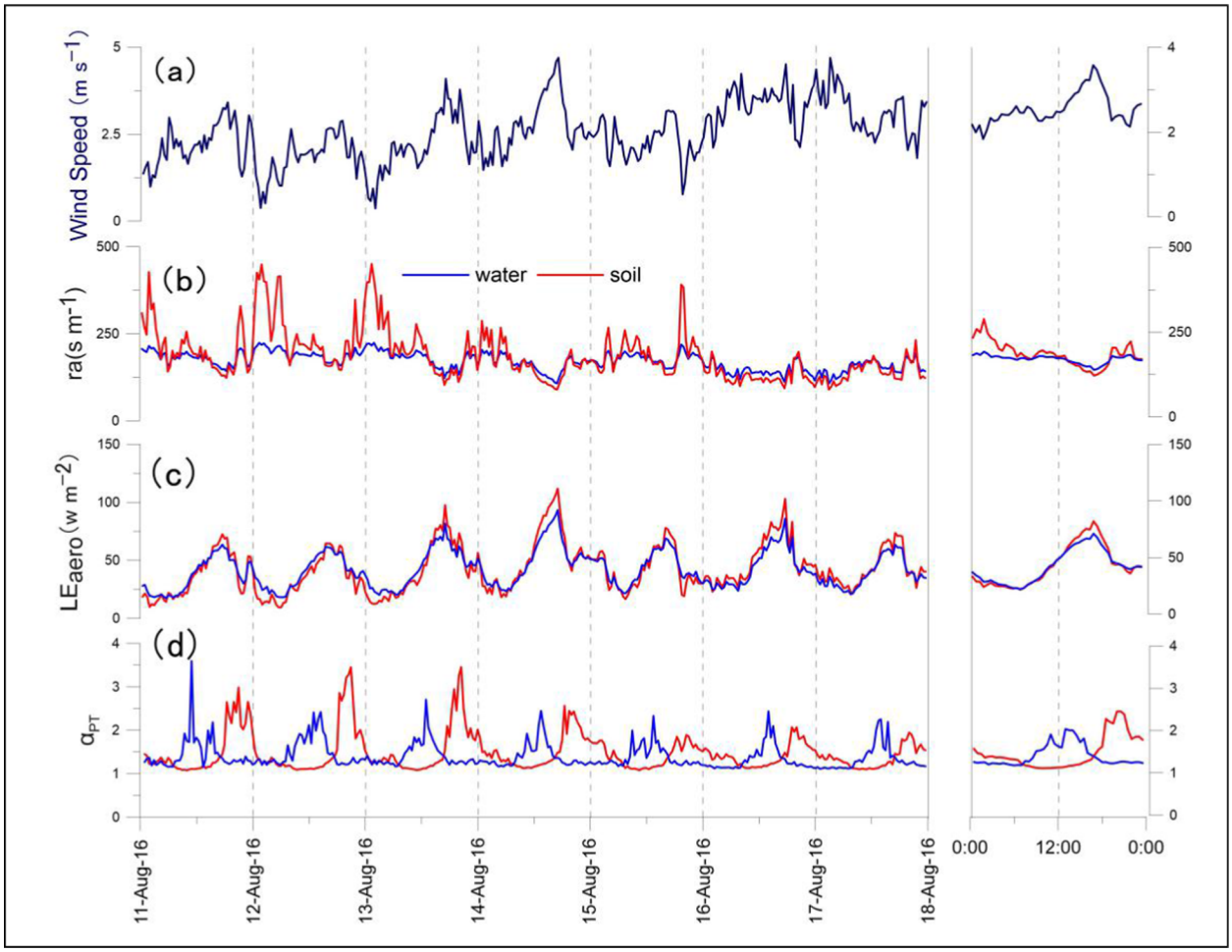

Fig. 13. Time series of wind speed (a), aerodynamic resistance (b), aerodynamic resistance term to evaporation LE_{aero} (c), and parameter α_{PT} calculated by the Penman-Monteith equation (d), with their diurnal average cycles on the right.

Declaration of Competing Interest

The authors declare that they have no known competing financial interests or personal relationships that could have appeared to influence the work reported in this paper.

Acknowledgments

We greatly appreciate the anonymous reviewers for their constructive comments. We also thank the assistance of Xiong Nie and Xiaona Qu in experiments and data collection.

Funding sources

This study is supported by:

The National Nature Science Foundation of China. (Nos. U1603243, 2018YFC0406504, 41230314).

Key Research and Development Program of Shaanxi Province (Program No. 2019DLSF05-01, Grant No. 2020SF-425).

SAFEA: Program for the Introduction of Renowned Overseas Professors (NO. MS2017CADX035).

Chang' an University Short-Term Study Abroad Program for Postgraduate Students (300104190103).

Appendix

Calculation of net radiation R_n

For soils, the net radiation can be expressed as:

$$R_{n,s} = R_{ns} + R_{nl} = (1 - \chi)\cdot R_{sd}\downarrow + (\varepsilon_s \cdot R_{ld}\downarrow - R_{lu}\uparrow) \quad (17)$$

$R_{n,s}(W\cdot m^{-2})$ is net radiation into soil, $R_{ns}(W\cdot m^{-2})$ is the net shortwave radiation, $R_{nl}(W\cdot m^{-2})$ is the net longwave radiation, $R_{sd}\downarrow(W\cdot m^{-2})$ and $R_{ld}\downarrow(W\cdot m^{-2})$ are the incoming shortwave and longwave radiation which are directly obtained from the meteorological station. ε_s is the reflection coefficient of longwave radiation and $R_{lu}\uparrow$ is the outgoing longwave radiation according Eq. (21) (Jensen and Allen, 2016). χ is surface albedo, and can be estimated based on surface water content (van Bavel and Hillel, 1976; Saito et al., 2006):

$$\begin{cases} \chi = 0.25 & \theta_{top} < 0.1 \\ \chi = 0.35 - \theta_{top} & 0.1 \leqslant \theta_{top} < 0.25 \\ \chi = 0.1 & \theta_{top} \geqslant 0.25 \end{cases} \quad (18)$$

$\chi = 0.1$ is used for a saturated bare surface. ε_s can be determined as:

$$\varepsilon_s = \min(0.9 + 0.18\theta_{top}; 1.0) \quad (19)$$

For water, the net radiation is calculated as:

$$R_{n,w} = R_{sd}\downarrow - R_{su}\uparrow + R_{ld}\downarrow - R_{lu}\uparrow - R_a \quad (20)$$

$R_{n,w}(W{\cdot}m^{-2})$ is net radiation into water, $R_{sd}\downarrow$ and $R_{ld}\downarrow$ $(W{\cdot}m^{-2})$ are the incoming shortwave and longwave radiation from the meteorological station, $R_{su}\uparrow$ $(W{\cdot}m^{-2})$ and $R_{lu}\uparrow$ $(W{\cdot}m^{-2})$ are the outgoing shortwave and longwave radiation, usually $R_{su}\uparrow = 0.1R_{sd}\downarrow$, $R_{lu}\uparrow = 0.03R_{ld}\downarrow$, $R_a(W{\cdot}m^{-2})$ is the longwave radiation emitted from the water body (Gianniou and Antonopoulos, 2007), given by:

$$R_a = 0.97{\cdot}\sigma{\cdot}(T + 273)^4 \quad (21)$$

where σ is the Stefan-Boltzman constant ($=5.67\times10^{-8}\ Wm^{-2}{\cdot}\ K^{-4}$), and T (°C) is the surface temperature (soil or water).

Calculation of G_s and N_w

For soils, heat flux G_0 can be calculated by using the Fourier law of heat conduction in a dimensional homogeneous medium by the gradient method:

$$G_0 = -\lambda{\cdot}\frac{T_j - T_{j-1}}{z_j - z_{j-1}} \quad (22)$$

where j is depth. The key point is identifying the thermal conductivity λ which can be calculated as:

$$\lambda = k{\cdot}c_s \quad (23)$$

where $k\,(m^2{\cdot}s^{-1})$ is the thermal diffusivity. The heat capacity c_s can be calculated using the following equation (organic content in soil is ignored):

$$c_s = c_{si}(1 - \theta_s) + c_{vw}{\cdot}\theta_s \quad (24)$$

where c_{si} is the volumetric heat capacity of dry fine sand, measured accurately by HOT DISK (0.970 MJ/m^3K), and c_{vw} is the volumetric heat capacity of water (4.18 MJ/m^3K), and θ_s is the saturated water content of fine sand (0.38). As a result c_s is equal to 2.19 MJ/m^3K.

Several methods have been proposed to parameterize k such as the amplitude method (AM), the phase shift method (PS), the conduction–convection method (CCM) and the harmonic method (HM). Results have shown that the high-order harmonic method is the best method to calculate k (An et al., 2016; Miao et al. 2012). The high-order harmonic method requires measured temperature data for at least three depths. The upper layer representes the top boundary for the Fourier series (Verhoef et al., 1996):

$$T(0, t) = \bar{T}(0) + \sum_{h=1}^{n} A_h \sin(\omega t + \sigma_h) \quad (25)$$

where $\bar{T}$ is the mean temperature, A_h is the amplitude, σ_h is the phase shift, and h is harmonic number. Soil temperature at depth z can be described as:

$$T(z, t) = \bar{T} + \sum_{h=1}^{n} A_h e^{-B_h{\cdot}\Delta z}{\cdot}\sin(h\omega t + \sigma_h - B_h{\cdot}\Delta z) \quad (26)$$

where ω $(rad{\cdot}s^{-1})$ is the rotation speed of the earth, also the frequency;Δz(m) the variation of depth; and B_h represents the influence of amplitude and phase variation at different depths, and can be expressed as:

$$B_h = \sqrt{\frac{h\omega}{2k}} \quad (27)$$

The second order model was chosen in this study, according to Miao (Miao et al., 2012). Using the nonlinear least squares method to fit the Fourier series resulted in estimates of the thermal parameters shown in Table 8.

Table 8
Heat diffusivity and conductivity of saturated fine sand.

Texture	Depth(cm)	$k(m^2{\cdot}s^{-1})$	$\lambda\ (W{\cdot}m^{-1}{\cdot}\ K^{-1})$
Fine Sand	3–5	4.89E-07	1.071

Table a
Summary of evaporation observation methods.

Method	Advantage	Disadvantage
Lysimeter	Direct, precise measurement	Representativeness, installation cost
Bowen ratio energy balance	Suitable for larger scale	Same turbulent diffusion coefficient for H and LE
Scintillometer	Suitable for larger scale	Applies field with uniform r_a
Eddy Covariance	Direct measurement	Energy closure problem, data discontinuity

Table b
List with meteorological measurement devices at site.

Variables	Commercial Name and Model for device	Company
Air temperature and humidity	Humidity and temperature sensors-083E-1–6	Met One Instrument
Net radiation components	Radiometer -CNR4	Kipp&Zonen
Wind speed	RM Young Wind Monitor	Campbell Scientific Inc.
Air pressure	Vaisala PTB110 Barometer-CS106	Campbell Scientific Inc.
Data logger	CR-3000	Campbell Scientific Inc.

Calculation of sensible heat flux H

The transfer of sensible heat flux from the surface into the atmosphere can be parameterized by resistance-type formulation using surface (soil or water) temperature T and air temperature T_a (Griend and Owe,1994; Stewart et al.,1994) according to flux-gradient theory (Cellier et al.,1996).

$$H = \frac{\rho \cdot c_p \cdot (T - T_a)}{r_a} \tag{28}$$

where $\rho(1.02\ kg \cdot m^{-3})$ is air density, c_p $(1010\ J \cdot kg^{-1} \cdot K^{-1})$ is the specific heat of air and $r_a(s \cdot m^{-1})$ is the aerodynamic resistance (Simunek et al., 2005; Brutsaert, 2013):

$$r_a = \frac{\left[\ln\frac{z_1 - d}{z_{om}} - \psi_m\right]\left[\ln\frac{z_2 - d}{z_{ov}} - \psi_v\right]}{k^2 \cdot u} \tag{29}$$

where k is the von Karman constant (0.4), $u(m \cdot s^{-1})$ is the wind speed, z_1 and z_2 are the measurement heights of wind speed and air temperature. For bare soils, the zero displacement height is zero (Griend and Owe,1994). z_{om} and z_{ov} are surface roughness lengths for momentum flux and heat flux, with values equal to 0.001 for bare soils (Simunek et al., 2005). ψ_m and ψ_v are the atmospheric stability correlation factor for momentum flux and heat flux (Bristow, 1987), for a well-watered reference surface. Stability correlation is normally not required because heat exchange is small (Allen et al., 1998; Ma et al., 2015). In this paper, the aerodynamic resistance for soil can be calculated as:

$$r_{a,s} = \frac{\left[\ln\frac{z_1 - d}{z_{om}}\right]\left[\ln\frac{z_2 - d}{z_{ov}}\right]}{k^2 \cdot u} \tag{30}$$

The aerodynamic resistance for the water surface can be calculated as:

$$r_{a,w} = \frac{4.72\left[\ln\left(\frac{z_1}{z_0}\right)\right]^2}{1 + 0.536 \cdot u} \tag{31}$$

where z_0 with value equal to 0.00137 is the aerodynamic roughness factor for water surface (Shuttleworth, 1993).

Calculation of other parameters

Saturation vapor pressure e_s (kPa) at air temperature can be calculated as (Zotarelli et al., 2010; Jensen and Allen, 2016):

$$e_s = 0.6108 \exp\left(\frac{17.27 \cdot T_a}{T_a + 237.14}\right) \tag{32}$$

In the Penman-Monteith model, Δ (kPa/°C) is the gradient of the "saturation" vapor pressure temperature curve, equation is recommended by FAO (Allen et al., 1998; Zotarelli et al., 2010; Jensen and Allen, 2016):

$$\Delta = \frac{4098 \cdot \left[0.6108 \exp\left(\frac{17.27 \cdot T_a}{T_a + 237.14}\right)\right]}{(T_a + 237.14)^2} \tag{33}$$

References

Allen, R.G., Jensen, M.E., Wright, J.L., Burman, R.D., 1989. Operational estimates of reference evapotranspiration. Agron. J. 81, 650–662.

Allen, R.G., Pereira, L.S., Raes, D., Smith, M., 1998. Crop evapotranspiration-Guidelines for computing crop water requirements-FAO Irrigation and drainage paper 56. Fao, Rome 300, D05109.

An, K., Wang, W., Wang, Z., Zhao, Y., Yang, Z., Chen, L., Zhang, Z., Duan, L., 2017. Estimation of ground heat flux from soil temperature over a bare soil. Theor. Appl. Climatol. 129, 913–922.

An, K., Wang, W., Zhao, Y., Huang, W., Chen, L., Zhang, Z., Wang, Q., Li, W., 2016.

Estimation from soil temperature of soil thermal diffusivity and heat flux in sub-surface layers. Bound.-Layer Meteorol. 158, 473–488.
Angus, D.E., Watts, P.J., 1984. Evapotranspiration — How good is the Bowen ratio method? Agric. Water Manage. 8, 133–150.
Arnon, A., Lensky, N.G., Selker, J.S., 2014. High-resolution temperature sensing in the Dead Sea using fiber optics. Water Resour. Res. 50, 1756–1772.
Bavel, C.H.M.V., 1966. Potential evaporation: the combination concept and its experimental verification. Water Resour. Res. 2, 455–467.
Blad, B.L., Rosenberg, N.J., 1974. Lysimetric calibration of the bowen ratio-energy balance method for evapotranspiration estimation in the central great plains. J. Appl. Meteorol. 13, 227–236.
Braud, I., Noilhan, J., Bessemoulin, P., Mascart, P., Haverkamp, R., Vauclin, M., 1993. Bare-ground surface heat and water exchanges under dry conditions: observations and parameterization. Bound.-Layer Meteorol. 66, 173–200.
Bristow, K.L., 1987. Soil physics with BASIC—transport models for soil plant systems : (Developments in Soil Science 14). Gaylon S. Campbell, Elsevier, Amsterdam/ Oxford/New York/Tokyo, 1985, xvi + 150pp., Dfl. 120.00, US $41.50 (hardcover), ISBN 0-444-42557-8. Agricultural & Forest Meteorology 41, 341–342.
Bruin, H.A.R.D., 1982. Temperature and energy balance of a water reservoir determined from standard weather data of a land station. J. Hydrol. 59, 261–274.
Brunner, P., Simmons, C.T., 2012. HydroGeoSphere: a fully integrated, physically based hydrological model. Groundwater 50, 170–176.
Brutsaert, W., 2013. Evaporation into the Atmosphere: Theory, History and Applications. Springer Science & Business Media.
Burt, C.M., Mutziger, A.J., Allen, R.G., Howell, T.A., 2005. Evaporation research: Review and interpretation. J. Irrig. Drain. Eng. 131, 37–58.
Carsel, R.F., Parrish, R.S., 1988. Developing joint probability distributions of soil water retention characteristics. Water Resour. Res. 24, 755–769.
Cellier, P., Richard, G., Robin, P., 1996. Partition of sensible heat fluxes into bare soil and the atmosphere. Agric. For. Meteorol. 82, 245–265.
Choudhury, B.J., Reginato, R.J., Idso, S.B., 1986. An analysis of infrared temperature observations over wheat and calculation of latent heat flux. Agric. For. Meteorol. 37, 75–88.
Crago, R.D., 1996. Comparison of the evaporative fraction and the Priestley-Taylor α for parameterizing daytime evaporation. Water Resour. Res. 32, 1403–1409.
Crago, R.D., Brutsaert, W., 1992. A comparison of several evaporation equations. Water Resour. Res. 28, 951–954.
Culf, A.D., Foken, T., Gash, J.H., 2004. The energy balance closure problem, in: Vegetation, Water, Humans and the Climate. Springer, pp. 159–166.
Devitt, D.A., Sala, A., Smith, S.D., Cleverly, J.R., Shaulis, L.K., Hammett, R., 1998. Bowen Ratio Estimates of Evapotranspiration for Tamarix ramosissima Stands on the Virgin River in Southern Nevada. Water Resour. Res. 34, 2407–2414.
Evett, S.R., Agam, N., Kustas, W.P., Colaizzi, P.D., Schwartz, R.C., 2012. Soil profile method for soil thermal diffusivity, conductivity and heat flux: comparison to soil heat flux plates. Adv. Water Resour. 50, 41–54.
Federer, C.A., Vörösmarty, C., Fekete, B., 1996. Intercomparison of methods for calculating potential evaporation in regional global water balance models. Water Resour. Res. 32, 2315–2321.
Finch, J.W., 2001. A comparison between measured and modelled open water evaporation from a reservoir in south-east England. Hydrol. Process. 15, 2771–2778.
Foken, T., 2008. The energy balance closure problem: an overview. Ecol. Appl. 18, 1351–1367.
Franssen, H.H., Stöckli, R., Lehner, I., Rotenberg, E., Seneviratne, S.I., 2010. Energy balance closure of eddy-covariance data: a multisite analysis for European FLUXNET stations. Agric. For. Meteorol. 150, 1553–1567.
Gallego-Elvira, B., Baille, A., Martin-Gorriz, B., Martínez-Alvarez, V., Maestre-Valero, J.F., 2011. Energy balance and evaporation loss of an irrigation reservoir equipped with a suspended cover in a semiarid climate (south-eastern Spain). Hydrol. Process. 25, 1694–1703.
Gavilán, P., Berengena, J., 2007. Accuracy of the Bowen ratio-energy balance method for measuring latent heat flux in a semiarid advective environment. Irrig. Sci. 25, 127–140.
Gianniou, S.K., Antonopoulos, V.Z., 2007. Evaporation and energy budget in Lake Vegoritis, Greece. J. Hydrol. 345, 212–223.
Goss, M.J., Ehlers, W., 2010. The role of lysimeters in the development of our understanding of soil water and nutrient dynamics in ecosystems. Soil Use Manage. 25, 213–223.
Granger, R.J., 1989. Examination of the concept of potential evaporation. J. Hydrol. (Amsterdam) 111, 9–19.
Griend, A.A.V.D., Owe, M., 1994. Bare soil surface resistance to evaporation by vapor diffusion under semiarid conditions. Water Resour. Res. 30, 181–188.
Hao, X., Li, W., Deng, H., 2016. The oasis effect and summer temperature rise in arid regions – case study in Tarim Basin. Sci. Rep. 6, 35418.
Heitman, J.L., Horton, R., Sauer, T.J., Ren, T.S., Xiao, X., 2010. Latent heat in soil heat flux measurements. Agric. For. Meteorol. 150, 1147–1153.
Hellwig, D.H.R., 1973. Evaporation of water from sand, 1: Experimental set-up and climatic influences. J. Hydrol. 18, 93–108.
Hollinger, D.Y., Richardson, A.D., 2005. Uncertainty in eddy covariance measurements and its application to physiological models. Tree Physiol. 25, 873–885.
Holmes, J.W., 1984. Measuring evapotranspiration by hydrological methods. Agric. Water Manage. 8, 29–40.
Horton, R., Wierenga, P.J., Nielsen, D.R., 1983. Evaluation of methods for determining the apparent thermal diffusivity of soil near the surface1. Soil Sci. Soc. Am. J. 47, 25.
Huntington, J.L., Szilagyi, J., Tyler, S.W., Pohll, G.M., 2011. Evaluating the complementary relationship for estimating evapotranspiration from arid shrublands. Water Resour. Res. 47, 143–158.
Jensen, M.E., Allen, R.G., 2016. Evaporation, evapotranspiration, and irrigation water requirements. American Society of Civil Engineers.
Kahler, D.M., Brutsaert, W., 2006. Complementary relationship between daily evaporation in the environment and pan evaporation. Water Resour. Res. 42 648-648.
Katul, G.G., Parlange, M.B., 1992. A Penman-Brutsaert model for wet surface evaporation. Water Resour. Res. 28, 121–126.
Kellner, E., 2001. Surface energy fluxes and control of evapotranspiration from a Swedish Sphagnum mire. Agric. For. Meteorol. 110, 101–123.
Kessomkiat, W., Franssen, H.H., Graf, A., Vereecken, H., 2013. Estimating random errors of eddy covariance data: an extended two-tower approach. Agric. For. Meteorol. 171, 203–219.
Kirono, D.G.C., Jones, R.N., Cleugh, H.A., 2010. Pan-evaporation measurements and Morton-point potential evaporation estimates in Australia: are their trends the same? Int. J. Climatol. 29, 711–718.
Lensky, N., Lensky, I.M., Peretz, A., Gertman, I., Tanny, J., Assouline, S., 2018. Diurnal course of evaporation from the dead sea in summer: a distinct double peak induced by solar radiation and night sea breeze. Water Resour. Res. 54.
Li, C.2018, Retrieved from: https://wenku.baidu.com/view/30e311ec85868762-caaedd3383c4bb4cf7ecb7af.html.
Liu, S., L, L., D, M., L, J., 2007. Evaluating parameterizations of aerodynamic resistance to heat transfer using field measurements. Hydrology and Earth System Sciences 11, 769–783.
Ma, N., Zhang, Y., Xu, C.Y., Szilagyi, J., 2015. Modeling actual evapotranspiration with routine meteorological variables in the data-scarce region of the Tibetan Plateau: comparisons and implications. J. Geophys. Res. Biogeosci. 120, 1638–1657.
Mahrt, L., 2010. Computing turbulent fluxes near the surface: needed improvements. Agric. For. Meteorol. 150, 501–509.
Mahrt, L., Ek, M., 1984. The Influence of atmospheric stability on potential evaporation. J. Appl. Meteorol. 23, 222–234.
Massman, W.J., 1993. Errors associated with the combination method for estimating soil heat flux. Soil Sci. Soc. Am. J. 57, 1198–1202.
Ma, Z., Wang, W., Zhang, Z., Brunner, P., Wang, Z., Chen, L., Zhao, M., Gong, C., 2019. Assessing bare-soil evaporation from different water-table depths using lysimeters and a numerical model in the Ordos Basin, China. Hydrogeol. J. 27, 2707–2718.
Mcilroy, I.C., 1984. Terminology and concepts in natural evaporation. Agric. Water Manage. 8, 77–98.
Mcjannet, D.L., Cook, F.J., Burn, S., 2013. Comparison of techniques for estimating evaporation from an irrigation water storage. Water Resour. Res. 49, 206–217.
Menenti, M., Choudhury, B.J., 1993. Parameteraization of land surface evaporation by means of location dependent potential evaporation and surface temperature range. In: Bolle, H.J., Feddes, R.A., Kalma, J.D. (Eds.), Exchange Processes at the Land Surface for a Range of Space and Time Scales. IAHS, Yokohama.
Miao, Y.C., Liu, S.H., Lu, S.H., Zhang, Y., 2012. A comparative study of computing methods of soil thermal diffusivity, temperature and heat flux. Diqiu Wuli Xuebao 55, 441–451.
Milly, P.C.D., 1992. Potential evaporation and soil moisture in general circulation models. J. Clim. 5, 209–226.
Monteith, J., Unsworth, M., 2008. Principles of Environmental Physics (Fourth Edition).
Morton, F.I., 1994. Evaporation research—a critical review and its lessons for the environmental sciences. Crit. Rev Environ. Sci. Technol. 24, 237–280.
Ochsner, T.E., Sauer, T.J., Horton, R., 2007. Soil heat storage measurements in energy balance studies. Agron. J. 99, 311–319.
Or, D., Lehmann, P., Shahraeeni, E., Shokri, N., 2013. Advances in soil evaporation physics—a review. Vadose Zone J. 12, 108–112.
Penman, H.L., 1948. Natural evaporation from open water, bare soil and grass. Proc. Royal Soc. London 193, 120–145.
Priestley, C.H.B., Taylor, R.J., 1972. On the assessment of surface heat flux and evaporation using large-scale parameters. Mon. Weather Rev. 100, 81–92.
Pütz, T., Fank, J., Flury, M., 2018. Lysimeters in vadose zone research. Vadose Zone J. 17.
Richardson, A.D., Braswell, B.H., Hollinger, D.Y., Burman, P., Davidson, E.A., Evans, R.S., Flanagan, L.B., Munger, J.W., Savage, K., Urbanski, S.P., 2006. Comparing simple respiration models for eddy flux and dynamic chamber data. Agric. For. Meteorol. 141, 219–234.
Roxy, M.S., Sumithranand, V.B., Renuka, G., 2014. Soil heat flux and day time surface energy balance closure at astronomical observatory, Thiruvananthapuram, south Kerala. J. Earth Syst. Sci. 123, 741–750.
Saito, H., Šimůneka, J., Mohantyb, B.P., 2006. Numerical analysis of coupled water, vapor and heat transport in the Vadose Zone. Vadose Zone J. 5, 784–800.
Scanlon, B.R., Tyler, S.W., Wierenga, P.J., 1997. Hydrologic issues in arid, unsaturated systems and implications for contaminant transport. Rev. Geophys. 35, 461–490.
Shah, N., Nachabe, M., Ross, M., 2007. Extinction depth and evapotranspiration from ground water under selected land covers. Groundwater 45, 329–338.
Shen, Y., Li, J., Wang, W., Deng, H., Wang, Z., 2014. Data acquisition device for automatic evaporation and precipitation measurement. CN203721111U.
Shuttleworth, W.J., 1993. Evaporation, Handbook of Hydrology, edited by: Maidment, DR. McGraw-Hill, New York.
Shuttleworth, W.J., 1983. Evaporation Models in the Global Water Budget.
Simunek, J., Van Genuchten, M.T., Sejna, M., 2005. The HYDRUS-1D software package for simulating the one-dimensional movement of water, heat, and multiple solutes in variably-saturated media. Univ. California-Riverside Res. Rep. 3, 1–240.
Singh, V.P., Xu, C.Y., 2015. Evaluation and generalization of 13 equations for determining free water evaporation. Hydrol. Process. 11, 311–323.
Stewart, J.B., Kustas, W.P., Humes, K.S., Nichols, W.D., Moran, M.S., de Bruin, H.A., 1994. Sensible heat flux-radiometric surface temperature relationship for eight semiarid areas. J. Appl. Meteorol. 33, 1110–1117.
Stewart, R.B., Rouse, W.R., 1977. Substantiation of the Priestley and Taylor parameter

$\alpha = 1.26$ for potential evaporation in high latitudes. J. Appl. Meteorol. 16, 649–650.
Tanner, B.D., 1988. Use requirements for Bowen ratio and eddy correlation determination of evapotranspiration, in: Planning Now for Irrigation and Drainage in the 21st Century. ASCE, pp. 605–616.
Tanner, C.B., Pelton, W.L., 1960. Potential evapotranspiration estimates by the approximate energy balance method of Penman. J. Geophys. Res. 65, 3391–3413.
Therrien, R., McLaren, R.G., Sudicky, E.A., Panday, S.M., 2010. A three-dimensional numerical model describing fully-integrated subsurface and surface flow and solute transportUser Guide. Retrieve from: https://www.ggl.ulaval.ca/fileadmin/ggl/documents/rtherrien/hydrogeosphere.pdf.
Trenberth, K.E., Fasullo, J.T., Kiehl, J., 2009. Earth's global energy budget. Bull. Am. Meteorol. Soc. 90, 311–324.
Van Bavel, C.H.M., Hillel, D.I., 1976. Calculating potential and actual evaporation from a bare soil surface by simulation of concurrent flow of water and heat. Agric. Meteorol. 17, 453–476.
van Genuchten, M.T., 1980. A closed-form equation for predicting the hydraulic conductivity of unsaturated soils 1. Soil Sci. Soc. Am. J. 44, 892–898.
Verhoef, A., Campbell, C.L., 2005. Evaporation Measurement.
Verhoef, A., van den Hurk, B.J., Jacobs, A.F., Heusinkveld, B.G., 1996. Thermal soil properties for vineyard (EFEDA-I) and savanna (HAPEX-Sahel) sites. Agric. For. Meteorol. 78, 1–18.
Viney, N.R., 1991. An empirical expression for aerodynamic resistance in the unstable boundary layer. Bound.-Layer Meteorol. 56, 381–393.
Wang, K., Dickinson, R.E., 2012. A review of global terrestrial evapotranspiration: observation, modeling, climatology, and climatic variability. Rev. Geophys. 50.
Westra, S., 2009. Hydroclimatology: perspectives and applications by ML Shelton.
Wilson, K., Goldstein, A., Falge, E., Aubinet, M., Baldocchi, D., Berbigier, P., Bernhofer, C., Ceulemans, R., Dolman, H., Field, C., 2002. Energy balance closure at FLUXNET sites. Agric. For. Meteorol. 113, 223–243.
Yang, K., Tamai, N., Koike, T., 2001. Analytical solution of surface layer similarity equations. J. Appl. Meteorol. 40, 1647–1653.
Yang, Y., Roderick, M.L., 2019. Radiation, surface temperature and evaporation over wet surfaces. Q. J. R. Meteorolog. Soc. 145, 1118–1129.
Zhidong, L., Shixiu, Y., Senchuan, X., 1988. Soil hydrodynamics. Tsinghua University Press, Beijing, China.
Zotarelli, L., Dukes, M.D., Romero, C.C., Migliaccio, K.W., Morgan, K.T., 2010. Step by step calculation of the Penman-Monteith Evapotranspiration (FAO-56 Method). Institute of Food and Agricultural Sciences. University of Florida.